



1           **Using nanoindentation to quantify the mechanical profile of Wufeng-Longmaxi**  
2           **formation shale in Southwest China: Link to sedimentary conditions**

3   Jianfeng Wang <sup>a, b\*</sup>, Chao Yang <sup>c\*\*</sup>, Yuke Liu <sup>d</sup>, Wenmin Jiang <sup>a</sup>, Yun Li <sup>a</sup>, Ting Zhang <sup>e, f</sup>, Yijun  
4   Zheng <sup>a</sup>, Yuhong Liao <sup>a</sup>, Qiuli Huo <sup>g, h, i</sup>, Li Fu <sup>g, h, i</sup>, Yusheng Wang <sup>g, h, i</sup>, Ping'an Peng <sup>a</sup>, Yongqiang  
5   Xiong <sup>a</sup>

6

7   a. State Key Laboratory of Deep Earth Processes and Resources, Guangzhou Institute of  
8   Geochemistry, Chinese Academy of Sciences, Guangzhou 510640, *PR* China

9   b. The Njord Centre, Departments of Geosciences and Physics, University of Oslo, Blindern, 0316  
10   Oslo, Norway

11   c. CAS Key Laboratory of Gas Hydrate, Guangzhou Institute of Energy Conversion, Chinese  
12   Academy of Sciences, Guangzhou 510640, *PR* China

13   d. Research Institute of Petroleum Exploration and Development, Beijing 100083, *PR* China

14   e. Key Laboratory of Petroleum Resources Research, Gansu Province, Lanzhou 730000, *PR* China

15   f. Research Center for Oil and Gas Resources, Northwest Institute of Eco-Environment and  
16   Resources, Chinese Academy of Sciences, Lanzhou 730000, *PR* China

17   g. Exploration and Development Research Institute of PetroChina Daqing Oilfield Co., Ltd.,  
18   Daqing 163712, *PR* China

19   h. State Key Laboratory of Continental Shale Oil, Daqing, 163712, *PR* China

20   i. Heilongjiang Provincial Key laboratory of Continental Shale Oil, Daqing, 163712, *PR* China

21   \* Corresponding Authors: Jianfeng Wang; [wangjianfeng@gig.ac.cn](mailto:wangjianfeng@gig.ac.cn); Chao Yang;

22   yangchao@ms.giec.ac.cn



23    **Abstract**

24        The fine construction of a continuous mechanical profile for the Wufeng to Longmaxi  
25 (WF-LMX) Formation sequence is crucial for designing hydraulic fracturing projects in shale gas  
26 development. However, the microscale mechanical profile of WF-LMX formation shale and its  
27 relationship to sedimentary conditions are poorly understood. This study investigates the  
28 mechanical profile of the WF-LMX Formation sequence using nanoindentation. A total of 27  
29 cutting samples were collected at one to one-half meter intervals from the Sanquan-1 well.  
30 Nanoindentation testing, rock mineralogy, major element analysis, and porosimetry were  
31 performed. The results showed that the WF-LMX shales in this study region were deposited in a  
32 passive continental margin environment, primarily from biogenic silica, in a warm and humid  
33 climate in a predominantly freshwater environment. Mechanical properties (hardness, fracture  
34 toughness, Young's modulus, and brittle index) varied synchronously with mineral and organic  
35 content across the vertical drilling profile, reflecting changes in lithology and sedimentary facies  
36 within the WF-LMX Formations. Shales in the upper part of the WF Formation and lower part of  
37 the LMX Formation, belonging to the deep-water shelf facies, exhibited high mechanical  
38 properties. Quartz and clay play a dominant role in controlling shale mechanics, while the minor  
39 rock constituents, nanoporosity have little effect. In particular, biogenic silica (authigenic quartz)  
40 plays an important role in increasing the brittleness of shale. The effect of shale constituents on  
41 micromechanics is essentially controlled by the sedimentary environment. Additionally, the  
42 potential of using nanoindentation to effectively assess shale brittleness was also demonstrated.  
43 This study provides a continuous and accurate interpretation profile of mechanical parameters and  
44 is helpful in determining favorable intervals for hydraulic fracturing in the design of shale gas



45 development.

46 **Keywords:** Wufeng-Longmaxi formation shale, sedimentary environment, mechanical profile,  
47 mineralogy, nanoindentation

48

## 49 **1 Introduction**

50 Shale gas is a significant unconventional hydrocarbon resource in China, and occurs in  
51 shale-dominated formations with low porosity and low permeability (Zou et al., 2010). Realizing  
52 commercial development of shale gas requires large-scale reservoir fracturing of shale formations  
53 (Guo et al., 2014). The optimal design of reservoir stimulation (i.e., hydraulic fracturing) highly  
54 depends on the reliable measurement of the mechanics of shale at different scales, which remains  
55 an ongoing challenge (Rickman et al., 2008, Sone and Zoback 2013a, b). In the past, the  
56 uniaxial/triaxial compression and the acoustic emission tests were the most common methods to  
57 investigate the mechanical properties of shale rock. These tests are conducted on centimeter-sized  
58 cores, thus obtaining shale mechanics at core scale. Although these macroscopic mechanical  
59 testing methods can provide reliable and directly applicable rock mechanics data for exploration  
60 and development, they are always flawed, especially when mechanical characterization of the  
61 entire shale formation is required to optimize favorable fracture intervals, since they rely on bulky  
62 core samples that are typically difficult to obtain (Alramahi and Sundberg 2012, Sone and Zoback  
63 2013a).

64 Nanoindentation, a technique widely used in micromechanical characterization, is  
65 increasingly being used to evaluate the micromechanical properties of shales (Ulm et al., 2005). It  
66 involves pressing a hard needle tip to press into the surface of the material, thus requiring small



67 sample volumes on the millimeter scale. Because drill cuttings (at the millimeter scale) can meet  
68 the requirements of nanoindentation mechanical testing and are readily available, the  
69 nanoindentation can achieve accurate mechanical characterization of the entire shale formation.  
70 By adjusting the indentation depth or applied load, elastic-plastic parameters such as hardness and  
71 Young's modulus of materials can be quickly derived from the load-displacement curves (Oliver  
72 and Pharr 1992). In addition, by developing mathematical models, scholars have also used  
73 indentation data to calculate other mechanical parameters, including fracture toughness  
74 characterizing the ability of a material to resist crack propagation, and brittleness index  
75 quantifying the fracturability of materials (Lawn and Marshall 1979, Ma et al. 2023). In order to  
76 determine the micromechanical properties of shales by nanoindentation, it is crucial to develop an  
77 appropriate indentation protocol, highlighting the importance of establishing a well-designed  
78 approach in this field, because shales have a more pronounced size effect and transverse  
79 heterogeneity at the microscale (Ulm and Abousleiman 2006, Wang et al., 2023, Yang et al., 2020).  
80 Currently, a statistical grid nanoindentation scheme is widely used, which is based on averaging a  
81 large amount of mechanical data from a series of indentations performed over a sufficiently large  
82 area and using large indentation loads (200-500 mN) (Abedi et al., 2016, Gupta et al., 2018, 2020,  
83 Kumar et al., 2012, Long et al., 2021, Shi et al., 2019a, 2019b, 2020, Shukla et al., 2013, Zhao et  
84 al., 2019). The use of a relatively large load is to indent a large volume to involve more matrix  
85 phases in each indentation (i.e., to reduce the impact of size effects), and the use of a  
86 nanoindentation campaign is to make the results more statistically significant (i.e., to reduce the  
87 impact of heterogeneity). A large number of indentation cases indicate that this method is reliable  
88 and scientific for obtaining the micromechanical properties of shale. Besides, some research



89 indicates that the Young's modulus determined by acoustic emission testing correlates well with  
90 measurements obtained by nanoindentation. (Kumar et al., 2012). In general, the mechanical  
91 properties (mainly Young's modulus) measured by nanoindentation can provides us with an  
92 efficient approach to analyze the mechanical properties and variation patterns of specific shale  
93 formation at the microscopic scale.

94 The Wufeng-Longmaxi (WF-LMX) Formation shales are the primary marine formations for  
95 shale gas exploration and development in southern China, with commercial developments  
96 successfully implemented in several locations including Fuling, Changning, and Weiyuan in  
97 Sichuan Province, China (Zou et al., 2010). In particular, the marine black shales of the WF-LMX  
98 Formation were predominantly deposited in a deep-water shelf environment characterized by  
99 strong reducing conditions (Zou et al., 2010). To date, extensive research has been conducted and  
100 documented on the geologic characteristics of areas conducive to WF-LMX shale gas  
101 accumulation (Guo and Zeng 2015, Yan et al., 2018, Zheng et al., 2022, Zou et al., 2010).  
102 Currently, engineering challenges have emerged as critical to the success of shale gas development.  
103 Among these, rock mechanics research, particularly as it relates to hydraulic fracturing, has been  
104 at the forefront of research efforts. Previous mechanical research on the WF-LMX shale was  
105 mainly based on macromechanical testing (Guo et al., 2019, Jia et al., 2021b). Although many  
106 significant achievements and insights have been made to guide exploration and production,  
107 several challenges remain, such as determining exactly how changes in stratigraphy correlate with  
108 changes in the mechanical properties of a shale sequence, which can then be used to identify the  
109 most suitable intervals for hydraulic fracturing operations (Sethi et al., 2024). Previous studies  
110 have attempted to use macroscopic testing to establish the relationship between macroscopic



111 mechanics and sedimentary conditions (Li et al., 2024, Sethi et al., 2024), while they are not able  
112 to characterize shale strata continuously and their inability to accurately depict the correlation  
113 between shale mechanics and sedimentary condition, especially for the fragile shale samples.  
114 Nanoindentation can overcome sampling problems, and a single mechanical test can  
115 simultaneously obtain these mechanical parameters. Recent literature mainly discusses the  
116 selection of indentation method (Du et al., 2021, Jia et al., 2021a, Shi et al., 2019b, Wang et al.,  
117 2022b), fluid influence (Yang et al., 2018, Yang et al., 2016), and component analysis of small  
118 sample size for the study of WF-LMX shale mechanics (Long et al., 2021). Few studies  
119 concerning the geological effects has been done for the micromechanical properties of shales  
120 (Charlton et al., 2023). To the best of our knowledge, there have been no investigations focusing  
121 on the microscale mechanical properties, namely elasticity, plasticity, toughness, and brittleness,  
122 of the marine shale of the WF-LMX formation along the southeastern margin of the Sichuan Basin  
123 and how these properties are related to sedimentary conditions.

124 In this study, we aim to use nanoindentation technology to perform a thorough mechanical  
125 characterization of WF-LMX shales at the microscale and to quantitatively assess the mechanical  
126 profile of WF-LMX shales. Specifically, in order to obtain micromechanical parameters, we  
127 particularly used a novel method to calculate the shale brittleness index based on nanoindentation  
128 data. Additionally, we aim to correlate the measured micromechanical data with the sedimentary  
129 conditions (e.g., redox condition and bedding) and rock physics (petromineralogy, reservoir space)  
130 of the WF-LMX formations. This correlation will enable us to identify the controlling factors of  
131 shale mechanics at the micro-scale and to investigate how lithofacies influence the  
132 micromechanical profile of WF-LMX shales. In general, this mechanical study of WF-LMX



133 shales in the whole layer using nanoindentation technique overcomes the limitations of traditional  
134 mechanical testing associated with sample availability. This approach provides a continuous and  
135 accurate interpretation profile of mechanical parameters for the design of shale gas development.

136

## 137 **2 Geological setting and sampling shale samples**

138 The Sichuan Basin and surrounding regions were characterized as stagnant basins during the  
139 Late Ordovician to Early Silurian, resulting in the formation of extensive low-energy and anoxic  
140 sedimentary environments (Chen et al., 2014). During this period, two significant global  
141 transgressions occurred, which contributed to extensive organic-rich shale intervals within the WF  
142 Formation and the bottom part of the LMX Formation (see Figure 1a). The black shale gradually  
143 shifted from the central sedimentary region to the source region (as shown in Figure 1a), while the  
144 paleoenvironment gradually evolved from deep-water shelf environments to semi-deep-water  
145 environments and finally to shallow-water shelf environments (Guo and Zeng 2015).

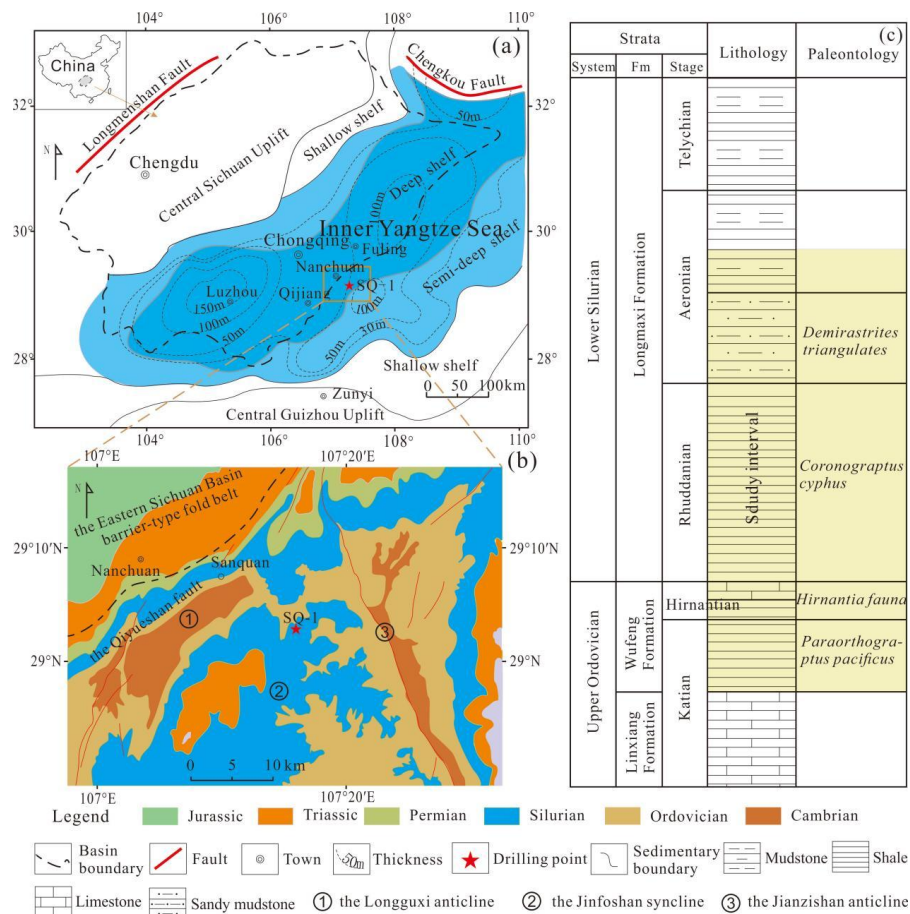


Figure 1. (a) shows a paleogeographic map of the Sichuan Basin and adjacent regions during the Early Silurian. (b) shows the regional, structural and geological profiles of the Sanquan region, highlighting the exposed strata and the Sanquan-1 well. (c) shows the stratigraphic, lithologic, and paleontologic column, along with the intervals under study (modified from (Zheng et al., 2018)).

Fm = Formation.

The Sanquan-1 (SQ-1) well, located in Sanquan Town, Nanchuan District, Chongqing City, within the Sichuan Basin of China (as shown in Figure 1b), is located on the crest of an anticline





155 and to the east of the Qiyue Shan Fault (see Figure 1b). Core shale samples were collected from  
156 the Upper Ordovician Wufeng Formation and the lower part of the Silurian Longmaxi Formation  
157 (as shown in Figure 1c). The stratigraphy of the SQ-1 well consists of muddy limestone, siliceous  
158 shale, carbonaceous shale, black shale, sandy mudstone and mudstone in sequence from base to  
159 top. According to biostratigraphy, petrography and gamma-ray (GR), sequence stratigraphy of  
160 Well SQ-1 can be distinguished (Figure 1c). There are two sections in the Longmaxi Formation of  
161 the SQ-1 well: the Rhuddanian and Aeronian stages. The Rhuddanian Stage, ranging from 60.5 to  
162 84.7 meters in depth, consists of black carbonaceous and black shale. The Aeronian Stage, from 11  
163 to 60.5 meters, consists of black shale and grayish-black argillaceous sandstone (Figure 1c). The  
164 WF Formation (84.7-90.0 m) contains two parts, the Katian Stage (86.0-90.0 m) and the  
165 Hernantian Stage (84.7-86.0 m) (Zheng et al., 2018).

166

### 167 **3 Samples and method**

#### 168 **3.1. Shale rock samples**

169 Shale core samples were systematically collected from the WF-LMX formation within the  
170 wellbore at intervals of one to one and one-half meters from the bottom up. A total of 27 core  
171 samples were collected for analysis. These samples have been used in previous geological and  
172 petrological studies targeting for shale gas exploration in WF-LMX shales (Yang et al., 2020,  
173 Zheng et al., 2018, 2022). Most of the information regarding total organic carbon (TOC)  
174 assessment, mineral composition analysis, major element analysis, experimental assessment of  
175 total porosity by mercury injection capillary pressure (MICP), and characterization of nanopore  
176 structures by N<sub>2</sub>/CO<sub>2</sub> gas adsorption techniques is provided in our previous research (Zheng et al.,



2018), and the related data can be found in Tables S1-S2. It is noted that previous studies of these samples have focused primarily on the organic geochemical properties, mineralogy, and porosity of the WF-LMX shale formations. In contrast, our research primarily investigates the coupling relationship between the micromechanical properties and the sedimentary environment of these shales.

### 3.2 Sample preparation

Shale samples were prepared with cuttings for nanoindentation test, generally 1-10 mm thick (Figure 2a). We chose shale samples oriented perpendicular to the bedding plane (designated X1) and those oriented parallel to the bedding plane (designated X3) (Figure 2b), first cut them into ~5 mm thick chips, then impregnated them and cemented them with resin, and ground and polished it using silicon carbide abrasive papers of various mesh sizes ranging from 50 to 2000 grit. This was followed by the application of diamond suspension fluid with particle diameters of 9, 3, and 1 micrometer for detailed polishing (Yang et al., 2020). Finally, an IM4000 argon ion mill was used for an additional 1-2 hours of polishing to achieve a very smooth surface. The average roughness (measured as root mean square roughness,  $R_q$ ) of the shale surface, which measures  $30 \times 30 \mu\text{m}^2$  and was measured using atomic force microscopy, is less than 100 nm (Wang et al., 2022b). Figure 2c shows a typical optical microscopy image of the shale sample after grid nanoindentation.



### 197 3.3 Optical microscopy

198 The mineralogy was examined using an Olympus 4500P optical microscope under reflected  
199 light, which was integrated with the nanoindentation system. This high-resolution optical  
200 microscope offers magnifications ranging from 200× to 4000×, making it suitable for precise  
201 visualization of the surface area prior to nanoindentation testing.

202

### 203 3.4 Scanning Electron Microscope (SEM)-Energy Dispersive Spectroscopy (EDS) imaging

204 Following the nanoindentation tests, we used a Hitachi S8010 Scanning Electron Microscope  
205 (SEM) integrated with Energy Dispersive Spectroscopy (EDS) to examine the indentations formed  
206 on the shale surface. Deviating from standard pre-treatment procedures, the specimens were not  
207 coated with a gold layer prior to testing to avoid potential damage to the indentation sites and to  
208 ensure unobstructed observation of the indentations. The phase distribution diagram based on  
209 elemental composition was quantified by EDS analysis.

210

211

### 212 3.5 Nanoindentation tests

#### 213 3.5.1 Nanoindentation and theoretical background

214 Mechanical nanoindentation tests were performed using an Anton Paar TTX NHT<sup>3</sup>  
215 nanoindenter with a diamond Berkovich indenter tip with a radius of curvature between 50 and  
216 100 nm (shown in Figure 2a). A high-resolution optical microscope was integrated into the  
217 indenter for precision. Loads ranging from 0.1 to 500 mN were applied to the indenter as it  
218 contacted and penetrated the sample surface.

219 Before performing the indentation tests, a standardized fused silicon sample was used to



220 calibrate the shape of the tip. Thanks to the unique reference ring design of the Anton Paar  
221 instrument, automatic thermal drift correction was implemented to ensure data stability. Figure 2d  
222 shows a schematic representation of the indentation profile, while Figure 2e shows a typical  
223 load-displacement curve ( $P$ - $h$  curve) consisting of three distinct phases: loading, holding and  
224 unloading. The loading phase includes both elastic and plastic deformation components, while the  
225 unloading phase captures only the elastic deformation-related strain recovery (Cheng et al., 2002,  
226 Yang et al., 2020). Consequently, the area under the unloading curve is referred to as the elastic  
227 energy ( $U_e$ ), and the area enclosed by both the loading and unloading curves represents the  
228 irreversible energy ( $U_p$ ). The total energy ( $U_t$ ) is the sum of  $U_e$  and  $U_p$  (Cheng et al., 2002). By  
229 analyzing the  $P$ - $h$  curve, the hardness ( $H$ ) and reduced elastic modulus ( $E_r$ ) of the shale will be  
230 derived (Oliver and Pharr 1992, 2004). In this investigation, a Poisson's ratio of 0.3 was assumed  
231 for the shale samples to calculate their Young's modulus ( $E$ ) (Li et al., 2018).

232

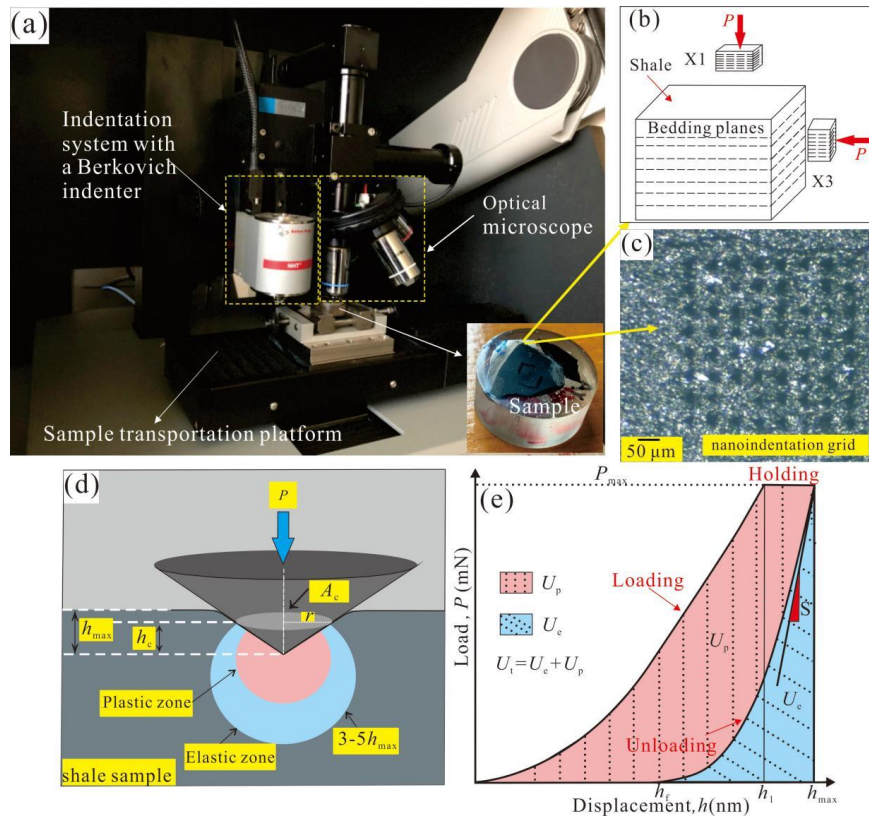


Figure 2. (a) The primary components of the nanoindenter are shown, with the polished specimen in the lower right corner. (b) shows the specimen with X1 and X3 planes, oriented differently for nanoindentation testing. (c) shows typical light microscopy images of a shale sample undergoing nanoindentation. (d) provides a schematic representation of the indentation profile. (e) shows a typical load-displacement ( $P$ - $h$ ) curve (modified from (Wang et al., 2023)). Here,  $P$  is the applied load,  $P_{\max}$  is the maximum load,  $r$  is the contact radius,  $S$  is the contact stiffness,  $h$  is the indentation displacement, while  $h_t$ ,  $h_1$ , and  $h_{\max}$  are the residual displacement, the displacement at the onset of the hold phase, and the maximum displacement during nanoindentation, respectively. The elastic-plastic deformation zone under the indenter is 3-5 times  $h_{\max}$  (Larsson et al., 1996).



### 244 3.5.2 Experimental protocols

245 Constant load holding tests were performed in which the indentation load was applied in a  
246 linear fashion until the peak load of 400 mN was reached. Once this peak load was reached, the  
247 diamond indenter was held in position for 2 seconds. Finally, the indentation test was completed  
248 with a 30-second unloading of the tip. We adopted the statistical nanoindentation method, which is  
249 widely used in the mechanical characterization of multi-phase composite materials (Figure 2c).  
250 Specifically, the peak load of 400 mN was used (Kumar et al., 2012). Each shale sample surface  
251 contained at least 7×7 grid indentations with the distance of at least 60 μm between adjacent  
252 indentations. Therefore, the size of the indentation areas was approximately 450 × 450 μm<sup>2</sup>, which  
253 is a much larger representative elementary area (REA) than that proposed by Liu et al. (2018) to  
254 ensure an unbiased statistical characterization. Prior to conducting the nanoindentation tests, we  
255 first observed the shale surface using a high-resolution optical microscope to determine the  
256 representative regions of interest, taking into account the multiscale heterogeneity and  
257 mineralogical variability of the shale. The shale surface areas selected for testing exhibited  
258 mineralogical characteristics consistent with the overall shale surface.

259

### 260 3.6 Determination of fracture toughness and brittleness index

261 In this study, the energy-based method was used to calculate the fracture toughness ( $K_{IC}$ ) of  
262 shale (Gautham and Sasmal 2022, Gupta et al., 2020, Liu, 2015, Liu et al., 2016, 2022, Liu 2015,  
263 Manjunath and Jha 2019, Zeng et al., 2017, Zeng et al., 2019). After we obtained  $K_{IC}$ , the  
264 brittleness index ( $B$ ) based on the mechanical properties can be calculated as (Lawn and Marshall  
265 1979):



266 
$$B = \frac{HE}{K_c} \quad (1)$$

267 The detailed calculation process can be found in the Test S1 of the Supplementary Material.

268

### 269 **3.7 Statistical Analyses**

270 Statistical significance of the correlations between mechanical parameters and mineralogy,  
271 TOC content, porosity and pore volume was determined by SPSS 23.0 software with Pearson  
272 correlation analyses and two-tailed Student's tests. This statistical analysis provides a range of  
273 correlation coefficients and tests designed to assess the magnitude and direction of the relationship  
274 between two variables. This allows us to gain a deeper insight into the patterns and relationships  
275 in the data, as well as to uncover potential associations that may go beyond the confines of simple  
276 linear correlations. All numerical analyses were performed using Origin 2021, Python 2.0 and  
277 Microsoft Excel 2016, and all graphs were made by Origin 2021, Corel Draw X8 and Microsoft  
278 Excel 2016.

279

## 280 **4 Results**

### 281 **4.1 Mineralogy and indentation of shale**

#### 282 **4.1.1 Optical properties of shale mineralogy**

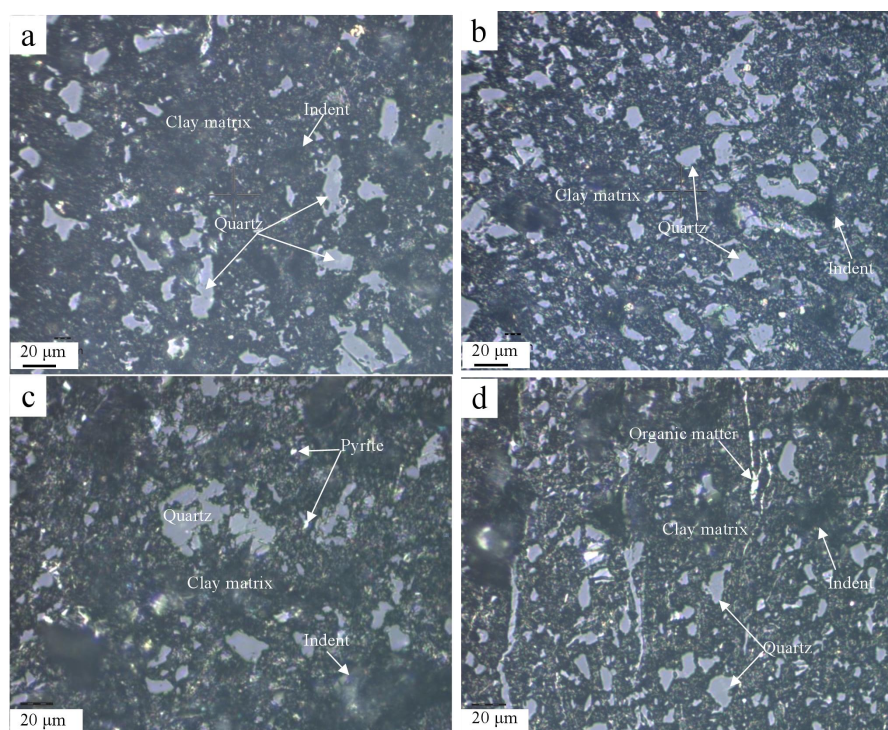
283 The core samples are mainly composed of quartz and clays ( $\geq 70$  vol.%) with small  
284 percentages of feldspar, carbonate, pyrite and organic matter. Here, we selected two representative  
285 samples (i.e., SQ-80b and SQ-90) in terms of their different mineralogical characteristics (i.e.,  
286 quartz-rich and clay-rich) to demonstrate the microstructure of the shale. The quartz grains present  
287 in the detrital material are translucent and have a grayish white color when viewed under reflected



288 light (Figure 3). They have a variety of irregular shapes characterized by sharp, straight  
289 boundaries and are predominantly between 15 and 40 microns in size (Figure 3). It is noteworthy  
290 that WF-LMX shales have large amount of authigenic quartz grains, which are usually very small  
291 in size, less than 2  $\mu\text{m}$ , and can only be orved by SEM (Milliken et al., 2016, Yang et al., 2020).  
292 The clay minerals show dark gray color and are continuously distributed in the shale matrix,  
293 constituting the connected skeleton of the shale (Figure 3). Notably, the clays are usually  
294 intermixed with nanometer-sized organic matter, forming the organoclay composites (Ma et al.,  
295 2015, Yang et al., 2020). Organic matter, consisting mostly of particles smaller than 3  $\mu\text{m}$ , is  
296 embedded in matrix voids or intermixed with clay minerals (Figure 3d). Pyrite typically appears as  
297 aggregates with dimensions ranging from 1 to 8  $\mu\text{m}$  (Yang et al., 2020). The pyrite and organic  
298 matter usually show a grayish white to bright white color under the reflected light. Overall, the  
299 quartz-rich shale sample has a coarse-grained texture with large mineral particles such as quartz  
300 acting as the supporting skeleton. However, the clay-rich shale has a continuous and fine-grained  
301 texture with organoclay composites acting as the framework materials of shale. Notably, the X1  
302 plane (as shown in Figures 4a and 4c) exhibits a lower amount of quartz compared to the X3 plane  
303 (as shown in Figures 4b and 4d).

304





305

306 Figure 3. Optical microscopy images of the mineralogy of the two representative shale samples.

307 The mineral composition characteristic for (a, b) quartz-rich shale, and (c, d) clay-rich shale. The

308 (a, c) are from X1 plane and (b, d) are from X3 plane. The X1 plane (a, c) of the shale sample has

309 a lower concentration of quartz grains compared to the X3 plane (b, d). The “indent” in (a, b, c and

310 d) represents the indentation residual impressions left in the shale.

311

#### 312 4.1.2 Nanoindentation of representative microdomains

313 Figure 4 displays the indents of SQ-78b sample in the X3 plane. Figure 4a shows the

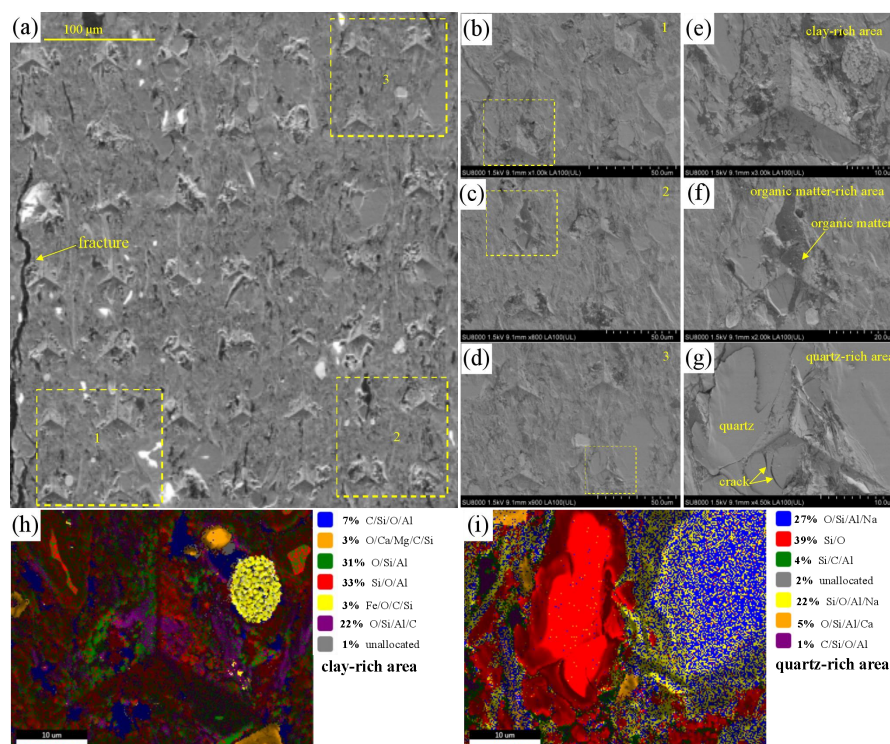
314 panorama of all the indentations. It is observed that some of the indents are located on

315 micro-fractures. Given the strong heterogeneity of the shale, we chose three representative

316 indentation areas for further analysis: the clay-rich area, the organic matter-rich area, and the



317 quartz-rich area. The quartz particle is large, and its surface is very smooth, mainly containing Si  
318 and O elements (Figures 4g and 4i). The organic matter in the backscattering diagram appears a  
319 black color (Curtis et al., 2012, Zhao et al., 2014), with no fixed form, and is shown in the form of  
320 small strips and thin threads (Figure 4f). The clay matrix often combines with the organic matter  
321 and mainly contains elements such as Al, Si, C and O (Figures 4e and 4h). The indentation  
322 impression in the quartz-rich area measures approximately 20  $\mu\text{m}$  in diameter, while those in the  
323 other two areas exceed 30  $\mu\text{m}$ . Microcracks are found around the quartz-rich area, indicating that  
324 quartz grain is fractured under the load of 400 mN. In contrast, no significant cracks are observed  
325 in the clay-rich and organic matter-rich areas. Furthermore, indentation impressions are clearly  
326 visible in the clay-rich and quartz-rich areas. In contrast, no indentation impressions are observed  
327 on the surface of the organic matter. This phenomenon has also been found in previous studies  
328 (Liu et al., 2019b, Wang et al., 2022a), and is attributed to the high elasticity of organic matter in  
329 the high maturity stage.



330

331 Figure 4. Backscattering (BSE) diagrams (a-g) and phase distribution diagram (h-i) of indent  
332 points in different regions. The numbers 1, 2, and 3 in (b-d) represent the corresponding enlarged  
333 parts. The phase distributions of (h-i) show the indentations are located on the clay-rich area and  
334 quartz-rich area, respectively. The indentation impression in the quartz-rich area has a diameter of  
335 about 20 μm, while the diameters of the other two areas are larger than 30 μm. The indent is  
336 clearly visible in the clay-rich or quartz-rich area, but not in the organic-rich area.

337

338 Figure 5 shows the *P-h* curves of all the indents and three typical indents. Figure 5a shows  
339 the maximum displacement ranges from ~3 to 6 μm. The indents present at the fracture zones (as  
340 shown in Figure 4) show significant displacements along with pop-in behavior characterized by  
341 abrupt jumps in displacement. This phenomenon could possibly be due to the development of



microcracks during the indentation process. The maximum indentation displacement in the quartz-rich area is significantly smaller than those in the organic-rich area (~4900 nm) and clay-rich area (~4900 nm). The E and H of the indentations in the quartz-rich area are the highest, with values of E=31.7 GPa and H=0.93 GPa, respectively, while those in the organic matter-rich area (E=26.7 GPa, H=0.85 GPa) and the clay-rich area (E=26.3 GPa, H=0.77 GPa) are lower (Table 1). Despite the relatively large differences in elasticoplastic parameters, the fracture toughness of these three indents is relatively similar, ranging from 0.79 MPa·m<sup>0.5</sup> to 0.85 MPa·m<sup>0.5</sup>. The B value for the indent of quartz-rich area is the highest (43.6 μm<sup>-1</sup>), followed by the indent in the clay-rich area (34.8 μm<sup>-1</sup>) and the indent in the organic matter-rich area (29.1 μm<sup>-1</sup>). Overall, the average mechanical parameters obtained are: E=29.4±3.2 GPa, H=0.95±0.41 GPa, K<sub>c</sub>=0.90±0.31 MPa·m<sup>0.5</sup>, and B=37.3±10.5 μm<sup>-1</sup>. Notably, the values of H show a larger variability (43.2% variation) than those of E (10.9 % variation) and K<sub>c</sub> (34.4 % variation).

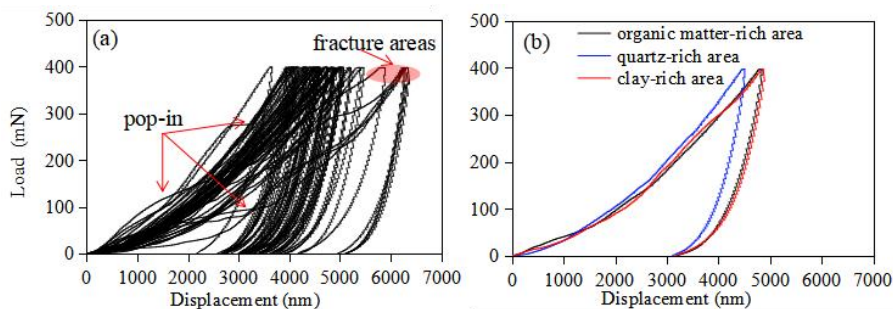


Figure 5. Load-displacement curve of (a) all the nanoindentation points, and (b) three typical indentation points in different areas.

Table 1. Mechanical parameters of nanoindentation points in different regions.

Point	Point of area	E (GPa)	H (GPa)	K <sub>c</sub> (MPa·m <sup>0.5</sup> )	B (μm <sup>-1</sup> )
-------	---------------	---------	---------	--	-----------------------



1st	Clay-rich	26.3	0.77	0.79	34.8
13th	Organic matter-rich	26.7	0.85	0.85	29.1
42th	Quartz-rich	31.7	0.93	0.82	43.6
All	All areas	29.4±3.2	0.95±0.41	0.90±0.31	37.3±10.5

360

## 361 4.2 TOC, mineralogy, porosity and major elemental characteristics

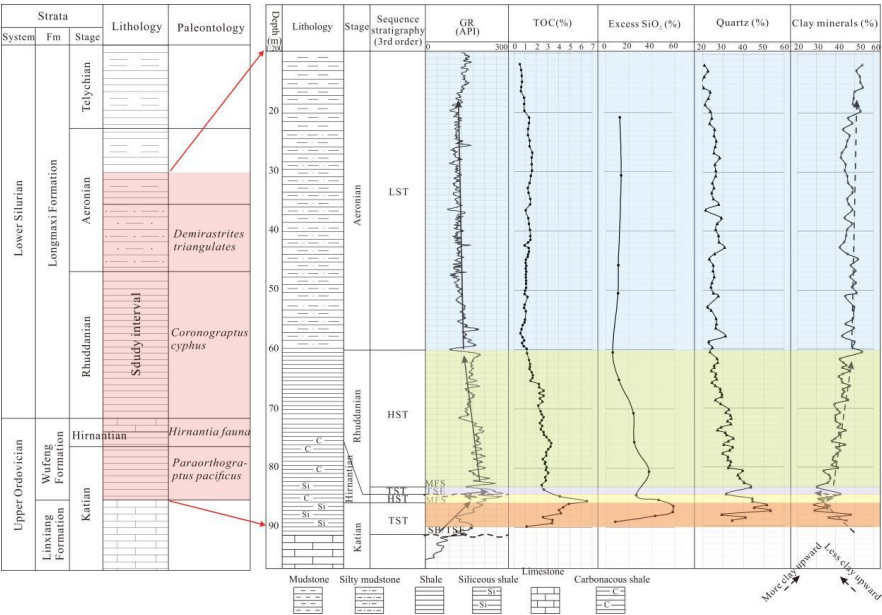
362 Using lithofacies analysis and gamma ray (GR) values, previous researchers have divided the  
363 WF Formation into two primary sections from base to top: the Transgressive Systems Tract (TST)  
364 and the Highstand Systems Tract (HST), while the LMX Formation was divided into TST, HST  
365 and LST (lowstand systems tract) from bottom to top for the SQ-1 well (Zheng et al., 2018)  
366 (Figure 6). The TOC content of LMX Formation and WF Formation are in the range of 0.53-3.34  
367 wt.% (average 1.94 wt.%) and 1.30-6.53 (average 3.74 wt.%), respectively. The quartz content  
368 values of LMX Formation and WF Formation are in the range of 19.6-43.6 vol.% (average 29.4  
369 vol.%) and 22.7-51.5 vol.% (average 39.3 vol.%), respectively. The clay content values of LMX  
370 Formation and WF Formation are in the range of 30.3-54.3 vol.% (average 43.1 vol.%) and  
371 28.8-48.1 vol.% (average 35.5 vol. %), respectively. Feldspar content ranges from 10.6 to 20.4  
372 vol%, with an average of 16.2 vol%. Conversely, the carbonate and pyrite contents are minimal,  
373 typically less than 10 vol% (Table S1). The major oxides in the WF-LMX Formations are SiO<sub>2</sub>  
374 and Al<sub>2</sub>O<sub>3</sub>. Other major element concentrations were observed to be <7% (Table S2). The SiO<sub>2</sub>  
375 content is the highest of all the oxides in the shale samples, ranging from 58.63% to 76.32%. The  
376 average SiO<sub>2</sub> content of WF Formation (69.73%) is higher than that of the LMX Formation  
377 (61.54%). The average Al<sub>2</sub>O<sub>3</sub> contents in LMX and WF Formations are 13.66% and 8.61%,  
378 respectively. The excess SiO<sub>2</sub> contents are in the range of 5.93-58.93% (Table S2).

379 As one moves upward through the drilling profile of the WF-LMX shales, the GR values and





380 TOC content initially increase and then decrease. The quartz content follows a similar pattern to  
381 the TOC content, while the clay mineral content shows an opposite trend. Excess silicon is widely  
382 distributed in the WF shales (Zheng et al., 2018). Previous research has shown that the excess  
383 silicon originates from authigenic silicon in shale, which is closely related to the genesis of  
384 siliceous plankton such as diatoms and sponge spicules in sedimentary waters (Schieber et al.,  
385 2000). In the SQ-1 well, the excess SiO<sub>2</sub> content varies from low at the bottom, to high in the  
386 middle, and then back to low at the top, with the higher values (ranging from 43.04% to 58.93%)  
387 being observed in the upper section of the WF Formation. In terms of reservoir space parameters,  
388 the total pore volume ( $V_{\text{total}}$ ) and total porosity exhibit ranges of  $21.0\text{--}41.4 \times 10^{-3} \text{ cm}^3/\text{g}$  and  
389 1.3–6.4%, respectively. The higher values are in the WF Formation, where the average values are  
390  $37.6 \times 10^{-3} \text{ cm}^3/\text{g}$  and 4.5%, respectively. In general, both  $V_{\text{total}}$  and total porosity are positively  
391 correlated with the TOC content (Table S1).



392  
393 Figure 6. A detailed histogram depicting various properties of the WF-LMX shales, including



394 gamma-ray (GR) intensity, TOC content, excess SiO<sub>2</sub> content, quartz content, and clay content  
395 (modified from Zheng et al. (2018)). HST is the highstand systems tract; LST is the lowstand  
396 systems tract; TST is the transgressive systems tract.

397

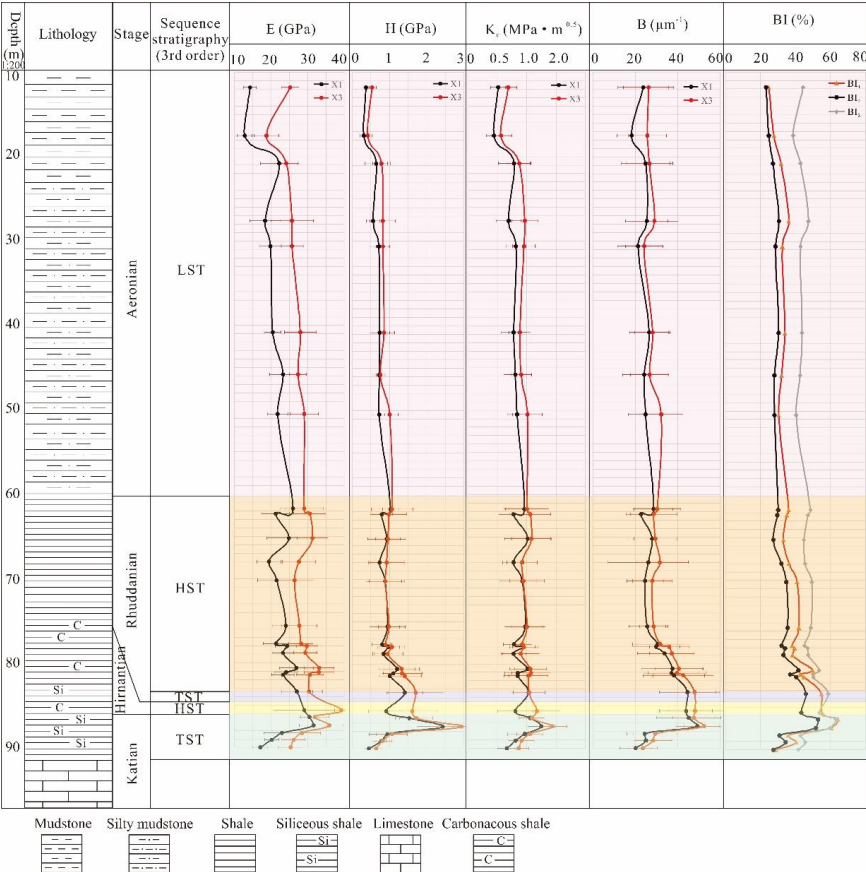
#### 398 **4.3 Micromechanical profile of WF-LMX shales**

399 Figure 7 shows the longitudinal variations of different micromechanical parameters (E, H, K<sub>c</sub>,  
400 and B) of WF-LMX Formations in the SQ-1 well. Table S3 presents the corresponding data.  
401 Overall, the mechanical parameters in the X1 plane change synchronously with those in the X3  
402 plane. Specifically, they first increase and then decrease from the bottom to the top, which is  
403 consistent with the variation of quartz and TOC content in the drilling profile. The highest  
404 mechanical property values occur in the Hirnantian and the upper Katian of the WF Formation  
405 (85-87.6 m), where the contents of TOC (4.2-6.5 wt.%) and quartz (44.4-53.3%) are also very  
406 high (Figure 6, Table 2). In fact, the WF Formation was in a deep-water marine shelf setting  
407 during the Hirnantian and the upper Katian stages. This leads to a significant enrichment of  
408 organic matter (possibly derived from siliceous organisms) in the WF shale. Conversely, the shales  
409 of the upper Aeronian stage of the LMX formation (SQ-11 and SQ-17), which belong to the  
410 shallow-water shelf facies, have the lowest mechanical values.

411 In general, the lower part of the Rhuddanian Stage of the LMX Formation and the Hirnantian  
412 and upper Katian stages of the WF Formation have higher values of E, H, and B. Table 2 indicates  
413 that the average values of micromechanical parameters (E, H, K<sub>c</sub>, and B) in the WF Formation are  
414 relatively higher than those in the LMX Formation. The micromechanical parameters (E, H, K<sub>c</sub>,  
415 and B) in the X1 plane are lower than those in the X3 plane.



416



417

418 Figure 7. A histogram of E, H, K<sub>c</sub> and BI (brittleness index) of shale in Well SQ-1. X1 indicates a  
419 direction perpendicular to the bedding plane of the shale, while X3 indicates a direction parallel to  
420 the bedding plane. BI<sub>1</sub>, BI<sub>2</sub>, and BI<sub>3</sub> are brittleness indices based on mineral composition (as  
421 shown in Table 4). From SQ-1 well bottom to the top, E, H, K<sub>c</sub>, and BI all show the similar trend,  
422 and the bottom of LMX Formation and the upper part of WF Formation (~80-87 m) have large  
423 values.

424





425 Table 2. Composition and micromechanical parameters of shale samples

Formation	TOC (wt. %)	Quartz (%)	Clay (%)	Carbonate (%)	Pyrite		Porosity (%)		E (GPa)		H (GPa)		K <sub>c</sub> (MPa m <sup>0.5</sup> )		B (μm <sup>-1</sup> )	
									X1	X3	X1	X3	X1	X3	X1	X3
Longmaxi	0.53-3.	19.6-43	30.3-54		1.6-6.	1.5-3.6			12.8-27	18.8-33	0.3-1.	0.4-1.	0.44-1.	0.56-1.	18.2-44	25.7-47
	34 (1.97)	.6 (29.6)	.3 (42.7)	5.1-10.7 (7.3)	8 (3.4)	(2.5)			.1 (21.9)	.1 (28.4)	4 (0.8)	7 (1.0)	03 (0.82)	07 (0.94)	.7 (28.4)	.9 (32.0)
Wufeng	1.30-6.	22.7-51	28.8-48		1.5-5.	2.9-6.4			17.1-31	25.3-39	0.4-2.	0.6-2.	0.66-1.	0.86-1.	20.1-49	23.5-52
	53 (3.74)	.5 (39.3)	.1 (35.5)	4.5-8.1 (5.6)	9 (2.5)	(4.5)			.6 (25.2)	.2 (31.1)	4 (1.2)	9 (1.4)	25 (0.92)	32 (1.09)	.3 (34.6)	.4 (38.2)

426  
427 Note: The mineral content is the volume percentage, and the data are expressed as: the lowest



428 value - the highest value (average value).

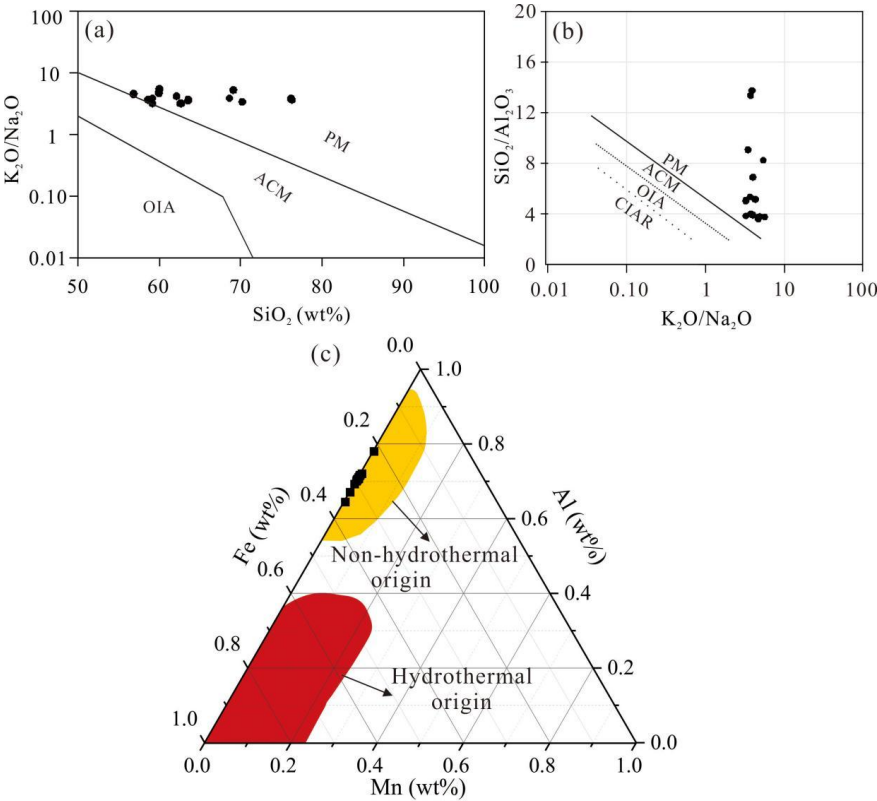
429

## 430 **5. Discussion**

### 431 **5.1 Paleo-depositional conditions of WF-LMX shales**

#### 432 **5.1.1 Sedimentary shale site**

433  $\text{Al}_2\text{O}_3$  and  $\text{TiO}_2$  are commonly used as indicators of terrigenous material, while Mn is  
434 considered a marker element from the deep ocean (Adachi et al., 1986, Boynton 1984). The  
435  $\text{MnO}/\text{TiO}_2$  ratio is generally less than 0.5 in coastal or continental shelf areas and ranges from 0.5  
436 to 3.5 in open ocean or deep sea environments (Adachi et al., 1986, Boynton 1984, Sethi et al.,  
437 2024). The average  $\text{MnO}/\text{TiO}_2$  value of 0.06 in the WF-LMX shales indicates a sedimentary  
438 environment closer to the continent. The  $\text{Al}_2\text{O}_3/(\text{Al}_2\text{O}_3+\text{Fe}_2\text{O}_3)$  ratios in sediments from ridge,  
439 basin, and continental margin areas are less than 0.4, in the range of 0.4 to 0.7, and between 0.7  
440 and 0.9, respectively (Murray et al., 1991). The  $\text{Al}_2\text{O}_3/(\text{Al}_2\text{O}_3+\text{Fe}_2\text{O}_3)$  ratio of WF-LMX shales  
441 ranges from 0.65 to 0.78, with an average of 0.71, suggesting a continental margin sedimentary  
442 environment. In addition, the  $\text{K}_2\text{O}/\text{Na}_2\text{O}$  vs.  $\text{SiO}_2$  and  $\text{SiO}_2/\text{Al}_2\text{O}_3$  vs.  $\text{K}_2\text{O}/\text{Na}_2\text{O}$  plots can also be  
443 used to determine the ancient and modern tectonic backgrounds of the basins (Roser and Korsch  
444 1988, Sethi et al., 2024). In Figure 8a-b, the WF-LMX shales show high  $\text{SiO}_2/\text{Al}_2\text{O}_3$  ratios,  
445  $\text{K}_2\text{O}/\text{Na}_2\text{O}$  ratios, and  $\text{SiO}_2$  values. The majority of the data points are within the passive  
446 continental margin. Therefore, the WF-LMX shales in the study area are indicative of a passive  
447 continental margin sedimentary environment.



448  
449 Figure 8. (a) Depositional position classification diagrams (a) (after Roser and Korsch. (1988))  
450 and (b) (after Maynard. (1982)). Identification origin of hydrothermal-biogenic sedimentary  
451 (Adachi et al., 1986). PM=passive continental margin; ACM=active continental margin;  
452 CIAR=continental island arc; OIA=oceanic island arc.

453  
454 **5.1.2 Sources of silicon**

455 Currently, the main sources of silicon in shales include biogenic, terrestrial detrital, and  
456 hydrothermal origins (Adachi et al., 1986, Reynolds and Verhoogen 1953).  $Al_2O_3$  is typically  
457 indicative of terrestrial detrital input. When the  $SiO_2/Al_2O_3$  ratio is close to 3, the silicon is  
458 primarily of crustal origin. However, when the ratio exceeds 3, silicon is primarily derived from



459 biogenic and hydrothermal processes (Boström et al., 1973). The  $\text{SiO}_2/\text{Al}_2\text{O}_3$  values of the  
460 WF-LMX shales range from 3.63 to 13.73 (with an average of 6.42), suggesting that silicon in  
461 these shale samples is not primarily derived from terrestrial detrital sources. In particular,  
462 geochemical proxies such as  $(\text{Fe} + \text{Mn})/\text{Ti}$  ratios above 25 ( $\pm 5$ ) and  $\text{Al}/(\text{Al} + \text{Fe} + \text{Mn})$  ratios  
463 below 0.35 are recognized as the presence of hydrothermal activity during deposition (Boström  
464 and Peterson 1969, He et al., 2016). The WF-LMX shale samples exhibit  $(\text{Fe} + \text{Mn})/\text{Ti}$  ratios  
465 ranging from 5.8 to 11.3, with an average of 8.9, while the  $\text{Al}/(\text{Al} + \text{Fe} + \text{Mn})$  ratios exhibit a  
466 narrower range of 0.64 to 0.78, with an average of 0.71 across the data set. This result indicates  
467 that silicon in the WF-LMX shale samples is not primarily derived from hydrothermal sources.  
468 Furthermore, by observing the Mn-Al-Fe ternary diagram (Figure 8c), all the sample data fall  
469 within the non-hydrothermal origin range. It is commonly believed that a  $\text{SiO}_2/\text{Al}_2\text{O}_3$  ratio  
470 exceeding 3.0 typically suggests a primarily biological origin (Boström et al., 1973). In the case of  
471 the WF-LMX shale samples, the  $\text{SiO}_2/\text{Al}_2\text{O}_3$  values varied between 3.63 and 13.34, with an  
472 average of 6.42. This indicates that the silica source in these shale samples was predominantly  
473 influenced by biogenic input.

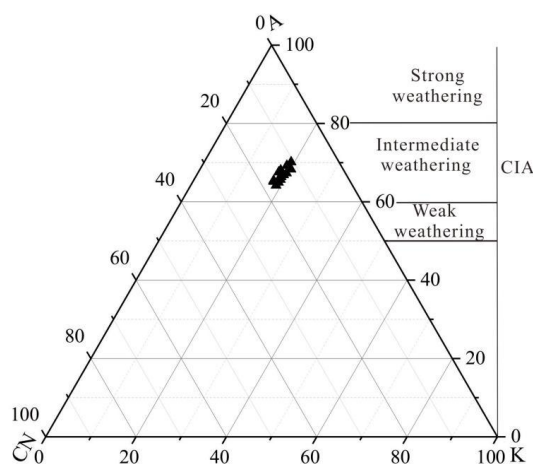
474

### 475 5.1.3 Paleoclimate and chemical weathering

476 The process of chemical weathering typically results in the depletion of elements such as Ca,  
477 Na, and K, while promoting the relative accumulation of Al and Ti (Fedo et al., 1995, Nesbitt and  
478 Wilson 1992). To quantify the extent of chemical weathering in sediment source areas, previous  
479 researches have established indices such as the Chemical Index of Alteration ( $\text{CIA} = 100 \times \text{Al}_2\text{O}_3 /$   
480  $(\text{Al}_2\text{O}_3 + \text{CaO}^* + \text{Na}_2\text{O} + \text{K}_2\text{O}))$  (Nesbitt and Wilson 1992, Nesbitt and Young 1982) and



481 Plagioclase index of alteration (PIA) ( $PIA = 100 \times (Al_2O_3 - K_2O) / ((Al_2O_3 - K_2O) + CaO^* +$   
482  $Na_2O)$ ) (Fedo et al., 1995). The units of the oxides used in these calculations are molar masses.  
483  $CaO^*$  refers specifically to the  $CaO$  content in silicate minerals. Since the  $CaO$  content in silicate  
484 minerals is often comparable to that of  $Na_2O$ , a correction method is applied: if the molar amount  
485 of  $CaO$  is greater than that of  $Na_2O$ ,  $CaO = Na_2O$ ; conversely, if the molar amount of  $CaO$  is less  
486 than that of  $Na_2O$ , no correction for  $CaO$  is required. In general, CIA values between 50-60 and  
487 PIA between 50-69 correspond to low weathering intensity, while CIA between 60-80 and PIA  
488 between 69-86 indicate moderate weathering, and CIA between 80-100 with PIA between 86-100  
489 represent intense weathering conditions (Li et al., 2024, Nesbitt and Young 1982, Reimann and de  
490 Caritat 2012). For the WF-LMX shale samples, the calculated CIA indices range from 64.2 to 70.2  
491 (mean = 65.9) (Figure 9; Table S2), and the PIA values range from 72.8 to 82.8 (mean = 76.94).  
492 These results indicate that the source rocks have experienced a consistent stable and moderate  
493 intensity of chemical weathering. In addition, the CIA index is commonly used to evaluate  
494 paleoclimatic conditions (Fedo et al., 1995, Nesbitt and Wilson 1992). In hot, humid paleoclimates,  
495 CIA indexes fluctuate between 80 and 100, while warm, humid environments show values  
496 between 60 and 80. Conversely, cold, arid paleoclimates generally record CIA values in the range  
497 of 50 to 60 (Nesbitt and Wilson 1992). The average CIA value of WF-LMX shale samples is 65.9,  
498 indicating deposition in warm and humid paleoclimatic conditions.



499

500 Figure 9. Ternary plots of  $\text{Al}_2\text{O}_3$  - ( $\text{CaO}^* + \text{Na}_2\text{O}$ )- $\text{K}_2\text{O}$  (A-CN-K) in molar proportions that  
501 reflecting the intensity of weathering (based map from (Nesbitt and Young 1982)). Here  $\text{CaO}^*$   
502 denotes the  $\text{CaO}$  content specifically within the silicate component.

503

#### 504 5.1.4 Paleosalinity and redox conditions

505 The  $\text{MgO}/\text{Al}_2\text{O}_3$  ratio is used to quantify the extent of historical salinity in aquatic systems  
506 (Zhang 1988, Zhou et al., 2022). Specifically,  $\text{MgO}$  is indicative of aquatic origins, whereas  $\text{Al}_2\text{O}_3$   
507 is indicative of terrestrial environments. Consequently, this ratio serves as a proxy for  
508 paleosalinity within water bodies. A value less than 1 indicates a freshwater environment, a range  
509 of 1 to 10 indicates a brackish water environment, and a ratio greater than 10 indicates a saline  
510 environment (Zhang 1988). Analysis of the shale samples shows  $\text{MgO}/\text{Al}_2\text{O}_3$  ratios ranging from  
511 0.14 to 0.20 ( mean = 0.17), indicating a freshwater depositional background. Previous studies  
512 have found that the redox indicators (e.g.,  $\text{U}/\text{Th}$ ,  $\text{Ni}/\text{Co}$ , and  $\text{Mo}$  values) of the WF-LMX shales  
513 are positively correlated with TOC content (Li et al., 2017, Yan et al., 2018). Based on the TOC  
514 content column profile of the SQ-1 well (Figure6), it can be inferred that the bottom of the LMX



515 Formation and the upper-middle part of the WF Formation had the strongest reducing conditions,  
516 with TOC content exceeding 2.5% formed in anoxic environments, while shale sections with TOC  
517 less than 2% were mainly formed in oxic environments. Furthermore, the high excess silicon  
518 content in organic-rich shales in the middle-upper part of the WF Formation and the bottom of the  
519 LMX Formation indicates relatively high paleoceanic productivity during deposition, which is  
520 consistent with previous findings (Li et al., 2017, Yan et al., 2018).

521

## 522 **5.2 Effect of components on micromechanical properties**

### 523 **5.2.1 Young's modulus, hardness, and fracture toughness**

524 The sedimentary environment controls the mineral composition, TOC content, and pore  
525 characteristics of organic-rich shales. Here we discuss the effect of constituents on the mechanical  
526 properties of WF-LMX shales. For both X1 and X3 planes, the linear positive correlation between  
527 Young's modulus of shale and the quartz content is good (Figure 10a). The reason is that quartz is  
528 thought to be a brittle mineral. The measured Young's modulus of bulk shale is enhanced by  
529 elevated concentrations of the quartz. In particular, Young's modulus of shale on both X1 and X3  
530 planes and the content of excess SiO<sub>2</sub> show a positive correlation, especially for that on the X1  
531 plane (Figure 10i). This means authigenic quartz plays an important role in increasing the strength  
532 of shale and improving the fracturability of the shale. Conversely, Young's modulus and clay  
533 mineral content show a negative correlation in different planes (Figure 10b).

534 As clay minerals inherently act as plastic components within shale matrices. While increased  
535 clay content decreases mechanical properties of shale, the scientific consensus remains unresolved  
536 regarding the brittle classification of feldspar, calcite, dolomite, and pyrite (Glorioso and Rattia



537 2012, Wang and Gale 2009).

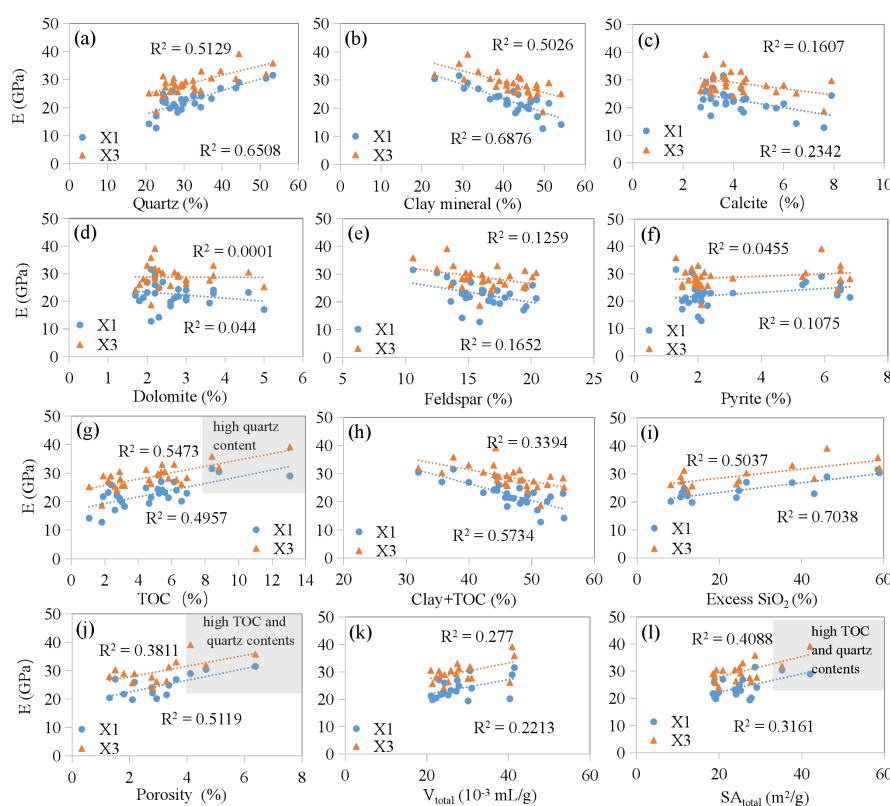
538 As shown in Figures 10c-10f, the content of these minerals do not show a direct positive  
539 relationship with Young's modulus values. Notably, there is a negative correlation between calcite  
540 content and modulus measurements (Table 3, Figure 10c), which is consistent with previous  
541 triaxial compression studies of core samples (Diao 2013). This phenomenon may be due to two  
542 factors: (1) relatively low calcite volume fractions (vol.% < 8%), and (2) isolated grain  
543 distribution patterns within the shale matrix. Such dispersed rigid particles (calcite, dolomite,  
544 pyrite) fail to form effective load-bearing frameworks, thereby precluding embrittlement  
545 enhancement by mineral reinforcement.

546 Compared to inorganic minerals, organic matter has lower density (approximately half the  
547 density of the shale rock minerals), and much lower modulus values in the range of 1-20 GPa  
548 (Fender et al., 2020, Wang et al., 2024). However, Young's modulus is statistically positively  
549 correlated with TOC content of WF-LMX shales in both planes (Figure 10g). The reason is that  
550 the contents of quartz and organic matter show a synchronous and co-directional trend in the  
551 stratigraphic profile. While organic matter inherently reduces shale strength, quartz emerges as the  
552 primary determinant in increasing shale Young's modulus, thereby leading to a consistent  
553 contribution relationship between organic matter and the Young's modulus of shale. Young's  
554 modulus shows no correlation with total nanopore volume or the total nanopore surface areas  
555 (Figure 10k-10l), and even a weak positive correlation with porosity (measured by MICP method)  
556 (Figure 10j). The main reason is that in the WF-LMX shale, high porosity and total pore volume  
557 are associated with high organic content (Table 3), which is positively correlated with the content  
558 of authigenic quartz. The influence of pores on shale mechanical properties may be compensated





559 by authigenic quartz. On the other hand, the relationship between Young's modulus and individual  
560 components shows a more pronounced correlation in the X1 plane compared to the X3 plane, a  
561 disparity that could be primarily due to the preferential orientation of mineral particles during  
562 sedimentation and the distinct mechanical behaviors inherent to their depositional environments.  
563



564  
565 Figure 10. Correlation of shale Young's modulus (E) with volumetric proportions of matrix  
566 constituents (a-h), excess SiO<sub>2</sub> content (i), porosity (j), total nanopore volume (k), and surface  
567 areas (l). Note: Q=Quartz, F=Feldspar, Car=Carbonate, Dol=Dolomite, Py=Pyrite, V<sub>total</sub>=the total  
568 nanopore volume, SA<sub>total</sub>=the total nanopore surface areas. The percentage of various components  
569 is the volume percentage. The marked three samples in (g and j) are in high quartz, TOC contents

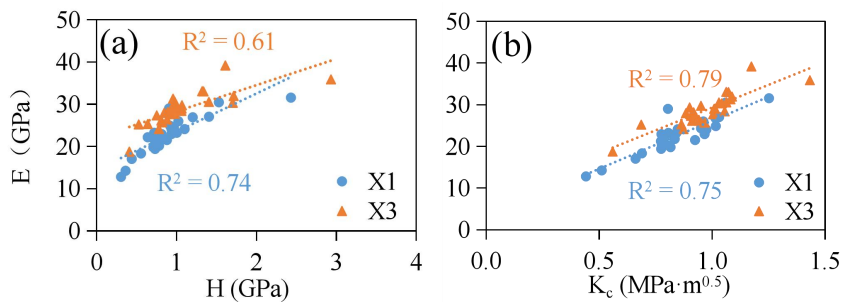


570 and porosity. Young's modulus shows high dependence on quartz, clay, and clay +TOC content,  
571 especially along the X1 plane, while it has weak or no correlation with the change in the content  
572 of other rock constituents, including the carbonates, organics and pores.

573

574 Figure 11 shows a good positive linear relationship between Young's modulus and both  
575 hardness and fracture toughness. The relationship between Young's modulus and hardness exhibits  
576 greater strength along the X1 plane ( $R^2=0.74$ ) compared to the X3 plane ( $R^2=0.60$ ). Conversely,  
577 the correlation between Young's modulus and fracture toughness maintains comparable  
578 magnitudes in both the X1 and X3 planes (Figure 11). Generally, the influence of components on  
579 hardness or fracture toughness is equivalent to that of Young's modulus. This observation may be  
580 due to the fact that Young's modulus serves as a direct measure of material stiffness, with higher  
581 values corresponding to increased resistance to deformation and crack propagation, thereby  
582 contributing to higher fracture toughness values (Gupta et al., 2020).

583



584

585 Figure 11. Relationships between E and (a) H, or (b) Kc.

586 Table 3 presents the statistical correlation analysis between the mechanical parameters and  
587 the mineralogical compositions, TOC content (volumetric fraction), porosity, and total pore



588 volume for the shale samples via SPSS software. Similar to the linear fit results observed in Figure  
589 10, the micromechanical properties ( $E$ ,  $H$ , and  $K_c$ ) of the WF-LMX shale show a good positive  
590 linear relationship with quartz, Q+Dol (quartz and dolomite), and QFC (quartz, feldspar, and  
591 carbonate) mineral assemblages, while exhibiting a negative correlation with clay mineral  
592 abundance and O/C (clay+TOC) composite content. Taken together, these relationships suggest  
593 that the micromechanical behavior of the shale is predominantly controlled by the proportional  
594 content of quartz, clay minerals, and organic-clay complexes, as these components form the  
595 primary structural framework of the shale matrix and collectively determine the overall  
596 mechanical performance of the WF-LMX formation.



Table 3. Correlation matrix to investigate the dependence of mechanical parameters on mineralogy, TOC content (volume fraction), porosity and pore volume.

	TOC	Qtz	Clay	F	Cal	Dol	Py	O/C	Q+Dol	QFC	$\phi$	PV <sub>total</sub>	E1	E3	H1	H3	K <sub>c1</sub>	K <sub>c3</sub>	B1	B3
TOC	1.00																			
Qtz	0.82	1.00																		
Clay	-0.79	-0.93	1.00																	
F	-0.57	-0.66	0.43	1.00																
Cal	-0.32	-0.31	0.26	-0.02	1.00															
Dol	-0.12	-0.12	0.05	0.37	-0.02	1.00														
Py	0.24	0.05	-0.23	0.00	-0.13	-0.38	1.00													
O/C	-0.57	-0.85	0.95	0.31	0.19	0.01	-0.18	1.00												
Q+Dol	0.82	1.00	-0.93	-0.63	-0.32	-0.03	0.01	-0.85	1.00											
QFC	0.60	0.77	-0.88	-0.07	-0.22	0.25	-0.02	-0.88	0.80	1.00										
$\phi$	0.72	0.56	-0.58	-0.40	-0.41	-0.39	0.16	-0.39	0.55	0.43	1.00									
PV <sub>total</sub>	0.81	0.60	-0.43	-0.66	-0.43	-0.28	-0.03	-0.16	0.58	0.24	0.59	1.00								
E1	<b>0.70</b>	<b>0.81</b>	<b>-0.83</b>	-0.41	-0.48	-0.21	0.33	<b>-0.77</b>	<b>0.79</b>	<b>0.65</b>	0.50	0.47	1.00							
E3	<b>0.75</b>	<b>0.72</b>	<b>-0.71</b>	-0.36	-0.40	-0.01	0.21	-0.58	<b>0.72</b>	<b>0.62</b>	0.37	0.50	0.84	1.00						
H1	0.57	<b>0.86</b>	<b>-0.79</b>	-0.53	-0.33	-0.17	0.05	<b>-0.78</b>	<b>0.85</b>	<b>0.67</b>	0.40	0.45	0.85	0.69	1.00					
H3	<b>0.66</b>	<b>0.89</b>	<b>-0.80</b>	-0.57	-0.33	-0.09	0.03	<b>-0.75</b>	<b>0.89</b>	<b>0.69</b>	0.32	0.52	0.83	0.78	0.96	1.00				
K <sub>c1</sub>	0.50	<b>0.69</b>	<b>-0.68</b>	-0.32	-0.46	-0.18	0.24	<b>-0.67</b>	<b>0.68</b>	0.57	0.55	0.32	0.89	0.65	0.88	0.77	1.00			
K <sub>c3</sub>	<b>0.63</b>	<b>0.73</b>	<b>-0.68</b>	-0.31	-0.54	-0.06	0.14	<b>-0.60</b>	<b>0.72</b>	<b>0.62</b>	0.44	0.53	0.86	0.86	0.84	0.87	0.84	1.00		
B1	<b>0.75</b>	<b>0.91</b>	<b>-0.90</b>	-0.57	-0.26	-0.06	0.18	<b>-0.84</b>	<b>0.91</b>	<b>0.74</b>	0.42	0.47	<b>0.83</b>	<b>0.81</b>	<b>0.82</b>	<b>0.89</b>	<b>0.64</b>	<b>0.71</b>	1.00	
B3	<b>0.75</b>	<b>0.91</b>	<b>-0.88</b>	-0.59	-0.21	-0.03	0.10	<b>-0.81</b>	<b>0.92</b>	<b>0.74</b>	<b>0.62</b>	0.47	<b>0.80</b>	<b>0.80</b>	<b>0.81</b>	<b>0.89</b>	<b>0.60</b>	<b>0.70</b>	<b>0.98</b>	1.00

Note: Qtz = quartz, F = feldspar, Cal = calcite, Dol = dolomite, Py = pyrite O/C = clay + TOC, QFC = total volume content of quartz, feldspar, and carbonate minerals,  $\phi$  = porosity, PV<sub>total</sub> = total nanopore volume, Superscripts 1 and 3 after mechanical parameters denote measurements along the parallel bedding plane (X1) and perpendicular bedding plane (X3), respectively.  $R^2 > 0.6$  are shown in bold. Negative signs (e.g. "-0.90") indicate inverse correlations between parameters. The micromechanical parameters (E, H, K<sub>c</sub>, and B) show strong dependencies on quartz abundance, clay content, O/C ratio, Q+Dol assemblage, and QFC mineral fractions, with nearly all correlation coefficients exceeding 0.60. This underscores their dominant control over the mechanical behavior of the shale.



5.2.2 Brittleness index

Table 3 shows that the B value based on micromechanical properties is strongly positively correlated with quartz ( $R^2=0.91$ ), Q+Dol ( $R^2\geq 0.91$ ) and QFC ( $R^2=0.74$ ) contents, and negatively correlated with clay ( $R^2\geq 0.88$ ), and clay+TOC contents ( $R^2\geq 0.81$ ). However, no significant correlations were observed between these parameters and other individual minerals, porosity, or total nanopore volume. Notably, the  $R^2$  values for the correlations between the brittleness index (B) and mineralogical constituents were similar to those for Young's modulus (E) and hardness (H), but had consistently higher magnitudes (Table 3). Therefore, quartz, especially for the authigenic quartz, as a distinct constituent of marine shale, plays an important role in enhancing the brittleness of shale. The B is strongly positively correlated with the E and H in both the planes, indirectly suggesting that the effect of component on B in shale is similar to that of E and H. To explain the accuracy of the brittleness index calculated based on micromechanical properties, mineral composition method and micromechanical properties based on nanoindentation method are compared to characterize the brittleness of shale. Due to the disunity of brittle minerals, three typical formulas based on mineral composition are each selected. Table 4 shows the brittle mineral and the corresponding formulas.

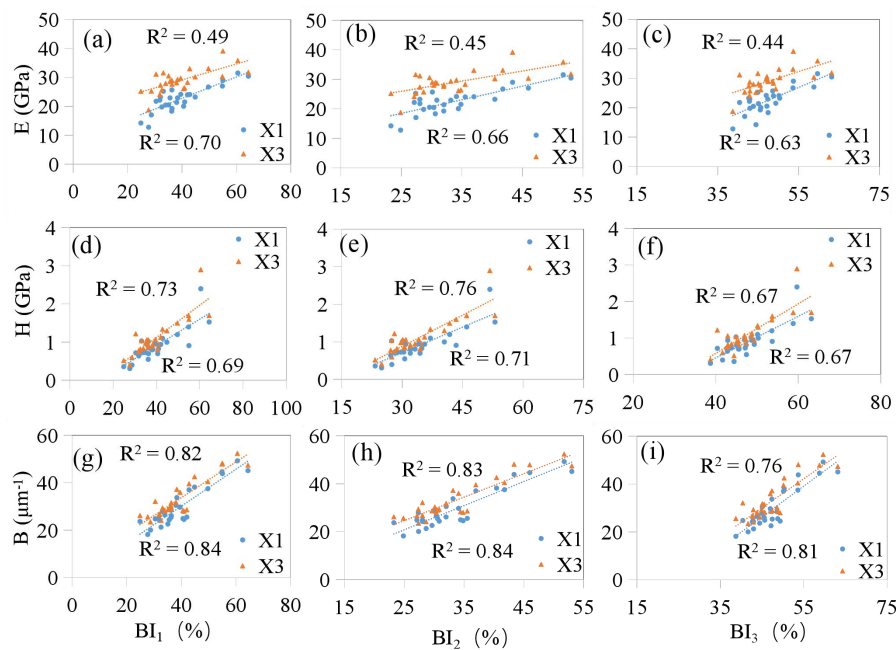
Table 4. Brittleness index model based on mineral composition (V=volume fraction).

Model	Equation	Brittle minerals	Reference
1	$BI_1=V_{Qtz}/(V_{Qtz}+V_{carb}+V_{clay})$	Quartz	Jarvie et al. (2007)
2	$BI_2=(V_{Qtz}+V_{Dol})/(V_{Qtz}+V_{carb}+V_{clay}+TOC)$	Quartz and dolomite	Wang and Gale (2009)
3	$BI_3=(V_{Qtz}+V_{carb})/(V_{Qtz}+V_{carb}+V_{clay}+TOC)$	Quartz and carbonate	Glorioso and Rattia (2012)

Figure 12 shows that the brittleness index has a better linear positive correlation with E along



the X1 plane than along the X3 plane. The correlations between  $BI_1$  and E are the strongest among the brittleness indices ( $BI_1$ ,  $BI_2$ , and  $BI_3$ ) along both the X1 ( $R^2=0.70$ ) and X3 planes ( $R^2=0.49$ ). The correlation between the brittleness index ( $BI_1$ ,  $BI_2$ , and  $BI_3$ ) and H in the X1 plane is close to that in the X3 plane. The correlations between the brittleness index ( $BI_1$ ,  $BI_2$ , and  $BI_3$ ) and H are almost all larger than those between E and the brittleness indices. This suggests that H in the X3 plane is more sensitive to the brittleness index than E. The reason may be related to the presence of various mineral phases and their overall physical properties. E is an inherent property of a material, fundamentally related to atomic bonds, while H measures the resistance to local plastic deformation caused by mechanical indentation or wear, which mainly depends on the microstructure or the arrangement of molecules and atoms (Liu et al., 2021). This difference may lead to the varying correlations with the brittleness index. The B value, determined from the micromechanical properties calculated from nanoindentation, exhibits a strong correlation with the mineral component-based  $BI_1$ ,  $BI_2$ , and  $BI_3$  values (Figures 12g-i). Moreover, it shows a similar trend of changes, from the base to the top of the SQ-1 well, as the  $BI_1$ ,  $BI_2$ , and  $BI_3$  values, indicating a high brittleness index at the lower interval of the LMX Formation and the upper interval of the WF Formation, between ~80.0-87.0 m (Figure 7). Compared with conventional logging data, we can predict the brittleness of shale in both X1 and X3 planes (Figure 7). Therefore, nanoindentation technology shows great potential in predicting the brittleness index of shale.



639

640 Figure 12. Relationship between Young's modulus (E), hardness, (H), brittleness index (B) based  
641 on the micromechanical properties and brittleness index (BI<sub>1</sub>, BI<sub>2</sub>, and BI<sub>3</sub>) based on mineral  
642 composition of shale

643

### 644 5.3 Relationship between micromechanical properties and sedimentary environment

645 For all studied shale samples, they were all deposited in a passive continental margin  
646 environment, the depositional period was characterized by a warm and humid climate and a  
647 predominantly freshwater environment. Therefore, these factors are not the main reasons for the  
648 change in micromechanical properties of WF-LMX shales. However, changes in constituents (e.g.,  
649 organic matter and biogenic silica), and redox conditions may have a significant effect on the  
650 variations in micromechanical properties of the shales. Previous studies have reported  
651 stratigraphic variations in mechanical properties of shales associated with different rock



652 mineralogy, which resulted from sea level cycles (Harris et al., 2011, Slatt and Abousleiman 2011),  
653 and were determined by the sedimentary environment. The WF Formation shales are located in a  
654 deep-water continental shelf sedimentary environment. They are located on a transgressive surface  
655 of erosion (TSE) or sequence boundary (SB) (Zheng et al., 2018). A decrease in clay minerals and  
656 an increase in organic matter and biogenic silica (excess SiO<sub>2</sub>) were observed in the transgressive  
657 system tract (TST) of the WF Formation from the lower to the upper part, which is likely due to  
658 the change in relative sea level and sediment supply (Liu et al., 2019a). Young's modulus,  
659 hardness, and brittleness increase in the TST. The increase in diagenetic silica upward through the  
660 TST is also found in the Devonian gas shales of the Appalachian Basin, which increases the  
661 brittleness (Lash and Blood 2011). The Young's modulus, hardness and brittleness increase almost  
662 throughout the TST until reaching up to the maximum flooding surface (MFS), and then decrease  
663 slightly in the highstand systems tract (HST) (Figures 6 and 7).

664 The lower section of the LMX Formation primarily occupies a deep-water continental shelf,  
665 characterized by low-energy and strong reduction conditions, resulting in the deposition of mainly  
666 gray-black shale. During the later stages of sedimentation in the LMX Formation, the sea level  
667 dropped, and the sedimentary environment gradually shifted to oxidizing conditions and turbidite  
668 sediments, leading to the development of a lithological combination dominated by sandy  
669 mudstone and muddy siltstone (Figure 1). The LMX Formation locates on a relatively thin  
670 carbonaceous shale TST (at the bottom of Rhudianian stage), thicker lowstand systems tract (LST)  
671 and highstand systems tract (HST). In general, organic matter and biogenic silica (quartz) decrease  
672 sharply from the basal to the upper intervals of Rhudianian stage of the LMX Formation, while  
673 they decrease slightly in the LST of Aeronian stage in the LMX Formation. Similarly, there is a





674 decrease in Young's modulus, hardness and brittleness in the HST, followed by a slight decrease in  
675 the LST. The HST in the LMX Formation records a large decrease in biogenic silica and organic  
676 matter input, which contributes to the decrease in hardness and brittleness. In contrast, the LST  
677 records a small decrease in silica and an increased flux of terrigenous clay minerals, resulting in a  
678 lower hardness and brittleness (Figures 6 and 7). In general, the elevated values of Young's  
679 modulus, hardness and brittleness values are in the middle upper part of the TST in the Katian  
680 stage, the HST, the TST in the Hirnantian stage and the bottom part of the HST in the Rhudanian  
681 stage, which belong to the deep-water shelf facies, corresponding to a high content of biogenic  
682 silica and organic matter, which may be the optimal intervals for hydraulic stimulation in these  
683 areas.

684

## 685 **6. Conclusions**

686 In this paper, we applied nanoindentation mechanical testing along with rock mineralogical,  
687 major elemental, and pore analyses to quantitatively evaluate the mechanical profile of WF-LMX  
688 shales, and the relationship between micromechanical properties and the sedimentary conditions  
689 of marine shale formations from the WF-LMX member in the shallow SQ-1 well, Sichuan Basin,  
690 Southwest China. The results were as follows:

691 (1) The WF-LMX shales within the study region were deposited in a passive margin  
692 environment. Biogenic silica was the major source. The sedimentation period was characterized  
693 by warm and humid climatic conditions, predominantly in a freshwater environment.

694 (2) The micromechanical properties varied synchronously with mineral and organic content  
695 across the vertical drilling profile, reflecting changes in lithology and sedimentary condition



696 within the WF-LMX Formations. Specifically, in the SQ-1 well, the micromechanical properties  
697 of the shales in the WF-LMX formation exhibit a distinct vertical pattern from bottom to top,  
698 sequentially passing through low, high and low intervals., which is relatively consistent with the  
699 variation of quartz and TOC content, whereas it is opposite to that of clay mineral content. We  
700 interpret these different trends as essentially dominated by the sedimentary environment of shale.

701 (3) Young's modulus shows a positive linear correlation with quartz content and TOC content,  
702 and a negative linear correlation with clay minerals, clay+TOC content. There are no or weak  
703 correlations with other individual minerals or porosity, suggesting that the micromechanical  
704 properties of LMX shale are primarily controlled by quartz content, clay minerals, and organoclay  
705 complexes. Autochthonous quartz contributes significantly to the elevated bulk Young's modulus  
706 values of the shale.

707 (4) The mineral content/Young's modulus relationship shows a stronger correlation in the X1  
708 plane compared to the X3 plane, and the influence of components in shale on hardness or fracture  
709 toughness is equivalent to that of Young's modulus.

710 (5) The mineralogy-based brittleness index exhibits a good positive linear correlation with  
711 both Young's modulus and hardness, with a slightly better correlation observed for hardness.  
712 Besides, the brittleness index based on micromechanical properties shows a significant  
713 consistency with the index based on mineral composition. Based on the nanoindentation method,  
714 the lower section of the LMX Formation and upper section of the WF Formation, belonging to the  
715 deep-water shelf facies, have high brittleness index values, potentially making them ideal intervals  
716 for hydraulic stimulation in relevant areas.

717 Our observations here demonstrate the relationship between micromechanical properties and



718 sedimentary environment of WF-LMX shale, and predict the optimal intervals for hydraulic  
719 stimulation of WF-LMX shale by the brittleness index based on micromechanical properties.  
720 Future research can verify the effectiveness of micromechanics in predicting shale fracture  
721 intervals by actual field logging data, such as dynamic Young's modulus, thus expanding the  
722 application scope of micromechanics in this field.

723

#### 724 **Acknowledgements**

725 This research was supported by the China Postdoctoral Science Foundation (2024M763277),  
726 the Postdoctoral Fellowship Program of CPSF (Grant No. GZC20241735), the National Natural  
727 Science Foundation of China (Grant No. 41802165 and Grant No. 42272182), the Basic and  
728 Applied Basic Research Project of Guangzhou City (Grant No. 2023A04J0208), and the Open  
729 Fund of Key Laboratory of Petroleum Resources Research, Gansu Province (SZDKFJJ2023009).  
730 The authors also thank Dr. Joanna Dziadkowiec and Prof. François Renard who for discussions.

731

#### 732 **Declaration of competing interest**

733 The authors declare that they have no known competing financial interests or personal  
734 relationships that could have appeared to influence the work reported in this paper.

735

#### 736 **Data availability**

737 The data that support the findings of this study are available from the corresponding author upon  
738 reasonable request.

739

#### 740 **Disclaimer**



741 Publisher's note: Copernicus Publications remains neutral with regard to jurisdictional claims in  
742 published maps and institutional affiliations.

743

#### 744 **Author contributions**

745 JW and CY were responsible for the design and methodology of the study, performed the  
746 experiments, assembled and analyzed the data, obtained and managed financial support, drafted  
747 and revised the paper. YL, WJ, YZ, and YL performed the experiments. YZ, QH, LF, YW, and YL  
748 collected the data. TZ, PP, and YX revised the draft. All authors contributed to the review of the  
749 article.

750

#### 751 **References**

752 Abedi, S., Slim, M., and Ulm, F.-J.: Nanomechanics of organic-rich shales: the role of thermal  
753 maturity and organic matter content on texture. *Acta Geotech.*, 11, 775-787.  
754 doi:10.1007/s11440-016-0476-2, 2016.

755 Adachi, M., Yamamoto, K., and Sugisaki, R.: Hydrothermal chert and associated siliceous rocks  
756 from the northern Pacific their geological significance as indication of ocean ridge activity.  
757 *Sediment. Geol.*, 47, 125-148. doi:[https://doi.org/10.1016/0037-0738\(86\)90075-8](https://doi.org/10.1016/0037-0738(86)90075-8), 1986.

758 Alramahi, B., and Sundberg, M. I.: Proppant Embedment And Conductivity of Hydraulic  
759 Fractures In Shales. Paper presented at the 46th U.S. Rock Mechanics/Geomechanics  
760 Symposium, 2012.

761 Boström, K., Kraemer, T., and Gartner, S.: Provenance and accumulation rates of opaline silica, Al,  
762 Ti, Fe, Mn, Cu, Ni and Co in Pacific pelagic sediments. *Chem. Geol.*, 11, 123-148.  
763 doi:[https://doi.org/10.1016/0009-2541\(73\)90049-1](https://doi.org/10.1016/0009-2541(73)90049-1), 1973.

764 Boström, K., and Peterson, M. N. A.: The origin of aluminum-poor ferromanganoan sediments in  
765 areas of high heat flow on the East Pacific Rise. *Mar. Geol.*, 7, 427-447.  
766 doi:[https://doi.org/10.1016/0025-3227\(69\)90016-4](https://doi.org/10.1016/0025-3227(69)90016-4), 1969.



- 767 Boynton, W.: Cosmochemistry of the Rare Earth Elements: Meteorite Studies. In D. i.  
768 Geochemistry (Ed.), 2, pp. 63-114. <https://doi.org/10.1016/B978-0-444-42148-7.50008-3>,  
769 1984.
- 770 Charlton, T., Rouainia, M., Aplin, A., Fisher, Q., and Bowen, L.: Nanoindentation of Horn River  
771 Basin Shales: The Micromechanical Contrast Between Overburden and Reservoir Formations.  
772 J. Geophys. Res.: Solid Earth, 128, e2022JB025957. doi:10.1029/2022JB025957, 2023.
- 773 Chen, X., Fan, J., Chen, Q., Tang, L., and Hou, X.: Toward a stepwise Kwangsi Orogeny.  
774 Science China Earth Sci. 57, 379-387. doi:10.1007/s11430-013-4815-y, 2014.
- 775 Cheng, Y. T., Li, Z., and Cheng, C. M.: Scaling relationships for indentation measurements. Philos.  
776 Mag. A, 82, 1821-1829. 2002.
- 777 Curtis, M. E., Cardott, B. J., Sondergeld, C. H., and Rai, C. S.: Development of organic porosity in  
778 the Woodford Shale with increasing thermal maturity. Int. J. Coal Geol., 103, 26-31.  
779 doi:<https://doi.org/10.1016/j.coal.2012.08.004>, 2012.
- 780 Diao, H.: Rock mechanical properties and brittleness evaluation of shale reservoir. Acta Petro. Sin.,  
781 29, 3300-3306. 2013.
- 782 Du, J., Whittle, A. J., Hu, L., Divoux, T., and Meegoda, J. N.: Characterization of meso-scale  
783 mechanical properties of Longmaxi shale using grid microindentation experiments. J. Rock  
784 Mech. Geotech. Eng., 13, 555-567. doi:10.1016/j.jrmge.2020.09.009, 2021.
- 785 Fedo, C., Nesbitt, H., and Young, G.: Unraveling the effects of potassium metasomatism in  
786 sedimentary rocks and paleosols, with implications for paleoweathering conditions and  
787 provenance. Geology, 23, 921-924.  
788 doi:10.1130/0091-7613(1995)023<0921:UTEOPM>2.3.CO;2, 1995.
- 789 Fender, T. D., Van Der Land, C., Rouainia, M., Graham, S. P., Jones, D. M., Vane, C. H., and  
790 Wagner, T.: The Assessment of Organic Matter Young's Modulus Distribution With  
791 Depositional Environment and Maturity. J. Geophys. Res.: Solid Earth, 125, e2020JB020435.  
792 doi:10.1029/2020jb020435, 2020.
- 793 Gautham, S., and Sasmal, S.: Nano-scale fracture toughness of fly ash incorporated hydrating  
794 cementitious composites using experimental nanoindentation technique. Theor. Appl. Fract.  
795 Mech., 117, 103180. doi:<https://doi.org/10.1016/j.tafmec.2021.103180>, 2022.
- 796 Glorioso, J. C., and Rattia, A.: Unconventional reservoirs: basic petrophysical concepts for shale



- 797 gas. Paper presented at the SPE. 153004, pp. 1-38, 2012.
- 798 Guo, T., and Zeng, P.: The Structural and Preservation Conditions for Shale Gas Enrichment and  
799 High Productivity in the Wufeng — Longmaxi Formation, Southeastern Sichuan Basin.  
800 Energy Explor. Exploit., 33, 259-276. 2015.
- 801 Guo, T., Zhang, S., Qu, Z., Zhou, T., Xiao, Y., and Gao, J.: Experimental study of hydraulic  
802 fracturing for shale by stimulated reservoir volume. Fuel, 128, 373-380.  
803 doi:<https://doi.org/10.1016/j.fuel.2014.03.029>, 2014.
- 804 Guo, W., Shen, W., Li, X., Wang, N., Liu, X., Zhang, X., and Zhou, S.: Study on mechanical  
805 characteristics and damage mechanism of the Longmaxi Formation shale in southern Sichuan  
806 Basin, China. Energy Explor. Exploit., 38, 454-472. doi:10.1177/0144598719876858, 2019.
- 807 Gupta, I., Sondergeld, C., and Rai, C.: Applications of NanoIndentation for Reservoir  
808 Characterization in Shales. In 52nd US Rock Mechanics/Geomechanics Symposium. 2018.
- 809 Gupta, I., Sondergeld, C., and Rai, C.: Fracture toughness in shales using nano-indentation. J.  
810 Petro. Sci. Eng., 191, 107222. doi:10.1016/j.petrol.2020.107222, 2020.
- 811 Harris, N., Miskimins, J., and Mnich, C.: Mechanical anisotropy in the Woodford Shale, Permian  
812 Basin: Origin, magnitude, and scale. The Leading Edge, 30, 284-291. doi:10.1190/1.3567259,  
813 2011.
- 814 He, C., Ji, L., Wu, Y., Su, A., and Zhang, M.: Characteristics of hydrothermal sedimentation  
815 process in the Yanchang Formation, south Ordos Basin, China: Evidence from element  
816 geochemistry. Sediment. Geol., 345, 33-41. doi:<https://doi.org/10.1016/j.sedgeo.2016.09.001>,  
817 2016.
- 818 Jarvie, D., Hill, R., Ruble, T., and Pollastro, R.: Unconventional shale-gas systems: The  
819 Mississippian Barnett Shale of north-central Texas as one model for thermogenic shale-gas  
820 assessment. AAPG bulletin, 91, 475-499. doi:10.1306/12190606068, 2007.
- 821 Jia, L., Xu, Q., and Zhang, L.: Assessment of deep shale fracture toughness using nanoindentation  
822 tests. IOP Conf. Ser.: Earth Environ. Sci, 861, 062068. doi:10.1088/1755-1315/861/6/062068,  
823 2021a.
- 824 Jia, Y., Tang, J., Lu, Y., and Lu, Z.: Laboratory geomechanical and petrophysical characterization  
825 of Longmaxi shale properties in Lower Silurian Formation, China. Mar. Pet. Geol., 124,  
826 104800. doi:<https://doi.org/10.1016/j.marpetgeo.2020.104800>, 2021b.



- 827 Kumar, V., Sondergeld, C. H., and Rai, C. S.: Nano to Macro Mechanical Characterization of  
828 Shale. Paper presented at the In SPE annual technical conference and exhibition, SPE 159804.  
829 <https://doi.org/10.2118/159804-MS>, 2012.
- 830 Larsson, P. L., Giannakopoulos, A. E., Sderlund, E., Rowcliffe, D. J., and Vestergaard, R.:  
831 Analysis of Berkovich indentation. *International Journal of Solids & Structures*, 33, 221-248.  
832 doi:10.1016/0020-7683(95)00033-7, 1996.
- 833 Lash, G., and Blood, R.: Sequence stratigraphy as expressed by shale source rock and reservoir  
834 characteristics—Examples from the Devonian succession, Appalachian Basin. *AAPG Search*  
835 *and Discovery*, 80168. 2011.
- 836 Laugier, M. T.: Palmqvist indentation toughness in WC-Co composites. *J. Mater. Sci. Lett.*, 6,  
837 897-900. doi:10.1007/BF01729862, 1987.
- 838 Lawn, B. R., and Marshall, D. B.: Hardness, Toughness, and Brittleness: An Indentation Analysis.  
839 *J. Am. Ceram. Soc.*, 62, 347-350. doi:<https://doi.org/10.1111/j.1151-2916.1979.tb19075.x>,  
840 1979.
- 841 Li, C., Ostadhassan, M., Abarghani, A., Fogden, A., and Kong, L.: Multi-scale evaluation of  
842 mechanical properties of the Bakken shale. *J. Mater. Sci.*, 54, 2133-2151.  
843 doi:10.1007/s10853-018-2946-4, 2018.
- 844 Li, H., Li, D., He, Q., Sun, Q., and Zhao, X.: Controlling mechanism of shale palaeoenvironment  
845 on its tensile strength: A case study of Banjiuguan Formation in Micangshan Mountain. *Fuel*,  
846 355, 129505. doi:<https://doi.org/10.1016/j.fuel.2023.129505>, 2024.
- 847 Li, Y., Zhang, T., Ellis, G. S., and Shao, D.: Depositional environment and organic matter  
848 accumulation of Upper Ordovician – Lower Silurian marine shale in the Upper Yangtze  
849 Platform, South China. *Palaeogeogr. Palaeoecol.*, 466, 252-264.  
850 doi:<https://doi.org/10.1016/j.palaeo.2016.11.037>, 2017.
- 851 Liu, B., Schieber, J., Mastalerz, M., and Teng, J.: Organic matter content and type variation in the  
852 sequence stratigraphic context of the Upper Devonian New Albany Shale, Illinois Basin.  
853 *Sediment. Geol.*, 383, 101-120. doi:<https://doi.org/10.1016/j.sedgeo.2019.02.004>, 2019a.
- 854 Liu, K., Jin, Z., Zeng, L., Ostadhassan, M., and Xu, X.: Understanding the creep behavior of shale  
855 via nano-DMA method. *Energy Rep.*, 7, 7478-7487.  
856 doi:<https://doi.org/10.1016/j.egyr.2021.10.099>, 2021.



- 857 Liu, K., Jin, Z., Zeng, L., Ozotta, O., Gentzis, T., and Ostadhassan, M.: Alteration in the  
858 mechanical properties of the Bakken during exposure to supercritical CO<sub>2</sub>. *Energy*, 262,  
859 125545. doi:<https://doi.org/10.1016/j.energy.2022.125545>, 2022.
- 860 Liu, K., Ostadhassan, M., and Bubach, B.: Applications of nano-indentation methods to estimate  
861 nanoscale mechanical properties of shale reservoir rocks. *J. Nat. Gas Sci. Eng.*, 35,  
862 1310-1319. doi:[10.1016/j.jngse.2016.09.068](https://doi.org/10.1016/j.jngse.2016.09.068), 2016.
- 863 Liu, Y.: Fracture toughness assessment of shales by nanoindentation. MS Thesis. University of  
864 Massachusetts Amherst. Cambridge, 2015.
- 865 Liu, Y., Xiong, Y., Liu, K., Yang, C., and Peng, P.: Indentation size and loading rate sensitivities on  
866 mechanical properties and creep behavior of solid bitumen. *Int. J. Coal Geol.*, 216, 103295.  
867 doi:<https://doi.org/10.1016/j.coal.2019.103295>, 2019b.
- 868 Long, Y., Zhang, Y., Huang, X., Wang, Y., Zhao, Y., Wang, R., and Song, F.: Assessment of the  
869 Multiphase Mechanical Properties of the Longmaxi Formation Shale Using Nanoindentation  
870 Tests. *ACS Omega*, 6, 18200-18214. doi:[10.1021/acsomega.1c02049](https://doi.org/10.1021/acsomega.1c02049), 2021.
- 871 Ma, Y., Zhong, N., Li, D., Pan, Z., Cheng, L., and Liu, K.: Organic matter/clay mineral  
872 intergranular pores in the Lower Cambrian Lujiaping Shale in the north-eastern part of the  
873 upper Yangtze area, China: A possible microscopic mechanism for gas preservation. *Int. J.*  
874 *Coal Geol.*, 137, 38-54. doi:<https://doi.org/10.1016/j.coal.2014.11.001>, 2015.
- 875 Manjunath, G. L., and Jha, B.: Geomechanical characterization of gondwana shale across  
876 nano-micro-meso scales. *Int. J. Rock Mech. Min. Sci.*, 119, 35-45.  
877 doi:<https://doi.org/10.1016/j.ijrmms.2019.04.003>, 2019.
- 878 Maynard, J. B., Valloni, R., & Yu, H.S. Composition of modern deep-sea sands from arc-related  
879 basins Geological Society of London Special Publications, 10, 551–561. 1982.
- 880 Milliken, K. L., Ergene, S. M., and Ozkan, A.: Quartz types, authigenic and detrital, in the Upper  
881 Cretaceous Eagle Ford Formation, South Texas, USA. *Sediment. Geol.*, 339, 273-288.  
882 doi:<https://doi.org/10.1016/j.sedgeo.2016.03.012>, 2016.
- 883 Murray, R. W., Buchholtz Ten Brink, M. R., Gerlach, D. C., Russ, G. P., and Jones, D. L.: Rare  
884 earth, major, and trace elements in chert from the Franciscan Complex and Monterey Group,  
885 California: Assessing REE sources to fine-grained marine sediments. *Geochim. Cosmochim.*  
886 *Acta*, 55, 1875-1895. doi:[https://doi.org/10.1016/0016-7037\(91\)90030-9](https://doi.org/10.1016/0016-7037(91)90030-9), 1991.





- 887 Nesbitt, H., and Wilson, R.: Recent Chemical Weathering of Basalts. *Am. J. Sci.*, 292, 740-777.  
888 doi:10.2475/ajs.292.10.740, 1992.
- 889 Nesbitt, H. W., and Young, G. M.: Early Proterozoic climates and plate motions inferred from  
890 major element chemistry of lutites. *Nature*, 299, 715-717. doi:10.1038/299715a0, 1982.
- 891 Oliver, W. C., and Pharr, G. M.: An improved technique for determining hardness and elastic  
892 modulus using load and displacement sensing indentation experiments. *J. Mater. Res.*, 7,  
893 1564-1583. doi:10.1557/JMR.1992.1564, 1992.
- 894 Oliver, W. C., and Pharr, G. M.: Measurement of hardness and elastic modulus by instrumented  
895 indentation: Advances in understanding and refinements to methodology. *J. Mater. Res.*, 19,  
896 3-20. 2004.
- 897 Reimann, C., and de Caritat, P.: New soil composition data for Europe and Australia:  
898 Demonstrating comparability, identifying continental-scale processes and learning lessons for  
899 global geochemical mapping. *Sci. Total Environ.*, 416, 239-252.  
900 doi:<https://doi.org/10.1016/j.scitotenv.2011.11.019>, 2012.
- 901 Reynolds, J. H., and Verhoogen, J.: Natural variations in the isotopic constitution of silicon.  
902 *Geochim. Cosmochim. Acta*, 3, 224-234. doi:[https://doi.org/10.1016/0016-7037\(53\)90041-6](https://doi.org/10.1016/0016-7037(53)90041-6),  
903 1953.
- 904 Rickman, R., Mullen, M., Petre, E., Grieser, B., and Kundert, D. (2008). A Practical Use of Shale  
905 Petrophysics for Stimulation Design Optimization: All Shale Plays Are Not Clones of the  
906 Barnett Shale. Paper presented at the SPE Annual Technical Conference and Exhibition.  
907 <https://doi.org/10.2118/115258-MS>
- 908 Roser, B. P., and Korsch, R. J.: Provenance signatures of sandstone-mudstone suites determined  
909 using discriminant function analysis of major-element data. *Chem. Geol.*, 67, 119-139.  
910 doi:[https://doi.org/10.1016/0009-2541\(88\)90010-1](https://doi.org/10.1016/0009-2541(88)90010-1), 1988.
- 911 Schieber, J., Krinsley, D., and Riciputi, L.: Diagenetic origin of quartz silt in mudstones and  
912 implications for silica cycling. *Nature*, 406, 981-985. doi:10.1038/35023143, 2000.
- 913 Sethi, C., Hazra, B., Ostadhassan, M., Motra, H. B., Dutta, A., Pandey, J. K., and Kumar, S.:  
914 Depositional environmental controls on mechanical stratigraphy of Barakar Shales in  
915 Rajmahal Basin, India. *Int. J. Coal Geol.*, 285, 104477.  
916 doi:<https://doi.org/10.1016/j.coal.2024.104477>, 2024.



- 917 Shi, X., He, Z., Long, S., Peng, Y., Li, D., and Jiang, S.: Loading rate effect on the mechanical  
918 behavior of brittle longmaxi shale in nanoindentation. *Int. J. Hydrogen Energy*, 44,  
919 6481-6490. doi:10.1016/j.ijhydene.2019.01.028, 2019a.
- 920 Shi, X., Jiang, S., Lu, S., He, Z., Li, D., Wang, Z., and Xiao, D.: Investigation of mechanical  
921 properties of bedded shale by nanoindentation tests: A case study on Lower Silurian  
922 Longmaxi Formation of Youyang area in southeast Chongqing, China. *Pet. Explor. Dev.*, 46,  
923 163-172. doi:10.1016/s1876-3804(19)30016-3, 2019b.
- 924 Shi, X., Jiang, S., Wang, Z., Bai, B., Xiao, D., and Tang, M.: Application of nanoindentation  
925 technology for characterizing the mechanical properties of shale before and after supercritical  
926 CO<sub>2</sub> fluid treatment. *J. CO<sub>2</sub> Util.*, 37, 158-172. doi:10.1016/j.jcou.2019.11.022, 2020.
- 927 Shukla, P., Kumar, V., Curtis, M., Sondergeld, C. H., and Rai, C. S.: Nanoindentation Studies on  
928 Shales. Paper presented at the 47th U.S. Rock Mechanics/Geomechanics Symposium, San  
929 Francisco, California, 2013.
- 930 Slatt, R. M., and Abousleiman, Y.: Merging sequence stratigraphy and geomechanics for  
931 unconventional gas shales. *The Leading Edge*, 30, 274-282. doi:10.1190/1.3567258, 2011.
- 932 Sone, H., and Zoback, M. D.: Mechanical properties of shale-gas reservoir rocks — Part 1: Static  
933 and dynamic elastic properties and anisotropy. *Geophysics*, 78, D381-D392.  
934 doi:10.1190/geo2013-0050.1, 2013a.
- 935 Sone, H., and Zoback, M. D.: Mechanical properties of shale-gas reservoir rocks — Part 2:  
936 Ductile creep, brittle strength, and their relation to the elastic modulus. *Geophysics*, 78,  
937 D390-D399. 2013b.
- 938 Ulm, F.J., and Abousleiman, Y.: The nanogranular nature of shale. *Acta Geotech.*, 1, 77-88.  
939 doi:10.1007/s11440-006-0009-5, 2006.
- 940 Ulm, F. J., Delafargue, A., and Constantinides, G.: *Experimental Microporomechanics*: Springer  
941 Vienna, 2005.
- 942 Wang, F. P., and Gale, J. F.: Screening criteria for shale-gas systems. *Gulf Coast Association of*  
943 *Geological Societies Transactions*, 59, 779-793. 2009.
- 944 Wang, J., Dziadkowiec, J., Liu, Y., Jiang, W., Zheng, Y., Xiong, Y., Peng, P. a., and Renard, F.:  
945 Combining atomic force microscopy and nanoindentation helps characterizing in-situ  
946 mechanical properties of organic matter in shale. *Int. J. Coal Geol.*, 281, 104406.



- 947       doi:<https://doi.org/10.1016/j.coal.2023.104406>, 2024.
- 948   Wang, J., Liu, Y., Yang, C., Jiang, W., Li, Y., Xiong, Y., and Peng, P. a.: Evolution of mechanical  
949       properties of kerogen with thermal maturity. *Mar. Pet. Geol.*, 145, 105906.  
950       doi:<https://doi.org/10.1016/j.marpetgeo.2022.105906>, 2022a.
- 951   Wang, J., Liu, Y., Yang, C., Zheng, Y., Jiang, W., Menegon, L., Renard, F., Peng, P. a., and Xiong,  
952       Y.: Upscaling the creep behavior of clay-rich and quartz-rich shales from nanoindentation  
953       measurements: Application to the Wufeng-Longmaxi shale, China. *Int. J. Rock Mech. Min.*  
954       *Sci.*, 171, 105580. doi:<https://doi.org/10.1016/j.ijrmms.2023.105580>, 2023.
- 955   Wang, J., Yang, C., Liu, Y., Li, Y., and Xiong, Y.: Using Nanoindentation to Characterize the  
956       Mechanical and Creep Properties of Shale: Load and Loading Strain Rate Effects. *ACS*  
957       *Omega*, 7, 14317-14331. doi:10.1021/acsomega.2c01190, 2022b.
- 958   Yan, C., Jin, Z., Zhao, J., Du, W., and Liu, Q.: Influence of sedimentary environment on organic  
959       matter enrichment in shale: A case study of the Wufeng and Longmaxi Formations of the  
960       Sichuan Basin, China. *Mar. Pet. Geol.*, 92, 880-894.  
961       doi:<https://doi.org/10.1016/j.marpetgeo.2018.01.024>, 2018.
- 962   Yang, C., Xiong, Y., Wang, J., Li, Y., and Jiang, W.: Mechanical characterization of shale matrix  
963       minerals using phase-positioned nanoindentation and nano-dynamic mechanical analysis. *Int.*  
964       *J. Coal Geol.*, 229, 103571. doi:10.1016/j.coal.2020.103571, 2020.
- 965   Yang, Z., Wang, L., Chen, Z., Xiang, D., Hou, D., Ho, C. L., and Zhang, G.: Micromechanical  
966       Characterization of Fluid/Shale Interactions by Means of Nanoindentation. *SPE Reservoir*  
967       *Eval. Eng.*, 21, 405-417. doi:10.2118/181833-pa, 2018.
- 968   Yang, Z., Wang, L., Zhang, G., and Ho, C.: Micromechanical characterization of fluid-shale  
969       interactions via nanoindentation. Paper presented at the SPE Asia Pacific Hydraulic  
970       Fracturing Conference, 2016.
- 971   Zeng, Q., Feng, Y., and Xu, S.: A discussion of " Application of nano-indentation methods to  
972       estimate nanoscale mechanical properties of shale reservoir rocks " by K Liu, M  
973       Osatadhasan and B Bubach. *J. Nat. Gas Sci. Eng.*, 42, 187-189.  
974       doi:10.1016/j.jngse.2017.02.027, 2017.
- 975   Zeng, Q., Wu, Y., Liu, Y., and Zhang, G.: Determining the micro-fracture properties of Antrim gas  
976       shale by an improved micro-indentation method. *J. Nat. Gas Sci. Eng.*, 62, 224-235.



- 977       doi:10.1016/j.jngse.2018.12.013, 2019.
- 978   Zhang, S.: Study on the Ratio of Mg and Al in Sedimentary Layer and its Application. Bull.
- 979       Mineralogy,Petrology Geochem.(in Chinese with English abstract), 1, 112-113. 1988.
- 980   Zhao, J., Zhang, D., Wu, T., Tang, H., and Dai, C.: Multiscale Approach for Mechanical
- 981       Characterization of Organic-Rich Shale and Its Application. Int. J. Geomech., 19, 04018180.
- 982       2019.
- 983   Zhao, X., Li, Q., Jiang, Z., Zhang, R., and Li, H.: Organic geochemistry and reservoir
- 984       characterization of the organic matter-rich calcilutite in the Shulu Sag, Bohai Bay Basin,
- 985       North China. Mar. Pet. Geol., 51, 239-255.
- 986       doi:<https://doi.org/10.1016/j.marpetgeo.2013.12.014>, 2014.
- 987   Zheng, Y., Liao, Y., Wang, Y., Xiong, Y., and Peng, P. a.: Organic geochemical characteristics,
- 988       mineralogy, petrophysical properties, and shale gas prospects of the Wufeng–Longmaxi
- 989       shales in Sanquan Town of the Nanchuan District, Chongqing. AAPG Bull., 102, 2239-2265.
- 990       doi:10.1306/04241817065, 2018.
- 991   Zheng, Y., Liao, Y., Wang, Y., Xiong, Y., and Peng, P. a.: The main geological factors controlling
- 992       the Wufeng-Longmaxi shale gas content. AAPG Bull., 106, 2073-2102.
- 993       doi:10.1306/07132218243 %J AAPG Bulletin, 2022.
- 994   Zhou, T., Zhou, Y., Zhao, H., Li, M., and Mu, H.: Depositional Setting and Enrichment
- 995       Mechanism of Organic Matter of Lower Cretaceous Shale in Ri-Qing-Wei Basin in the
- 996       Central Sulu Orogenic Belt. Front. Earth Sci., 9, 808916. doi:10.3389/feart.2021.808916,
- 997       2022.
- 998   Zou, C., Dong, D., Wang, S., Li, J., Li, X., Wang, Y., Li, D., and Cheng, K.: Geological
- 999       characteristics and resource potential of shale gas in China. Pet. Explor. Dev., 37, 641-653.
- 1000       doi:10.1016/s1876-3804(11)60001-3, 2010.
- 1001